Probing the Nature of Zinc in Copper−Zinc−Zirconium Catalysts by Operando Spectroscopies for CO_2 Hydrogenation to Methanol

Meng Yang[a,b], Jiafeng Yu*[a], Anna Zimina[c,d], Bidyut Bikash Sarma[c,d], Lakshmi Pandit[c,d], Jan-Dierk Grunwaldt*[d,c], Ling Zhang[a,b], Hengyong Xu[a], Jian Sun*[a]

[a] M. Yang, Dr. J. Yu, L. Zhang, Prof. H. Xu, Prof. Dr. J. Sun
Dalian Institute of Chemical Physics, Chinese Academy of Sciences
Zhongshan Road 457, 116023 Dalian (China)
E-mail: yujf@dicp.ac.cn, sunj@dicp.ac.cn
[b] M. Yang, L. Zhang
University of Chinese Academy of Sciences
100049 Beijing (China)
[c] Dr. A. Zimina, Dr. B. B. Sarma, Dr. L. Pandit, Prof. Dr. J.−D. Grunwaldt
Institute of Catalysis Research and Technology (IKFT), Karlsruhe Institute of Technology (KIT)
Hermann-von-Helmholtz-Platz 1, 76344 Eggenstein-Leopoldshafen (Germany)
E-mail: grunwaldt@kit.edu
[d] Dr. A. Zimina, Dr. B. B. Sarma, Prof. Dr. J.-D. Grunwaldt
Institute for Chemical Technology and Polymer Chemistry (ITCP), Karlsruhe Institute of Technology (KIT)
Engesserstraße 20, 76131 Karlsruhe (Germany)

Supporting information for this article is given via a link at the end of the document.

Abstract: Active Zn species in Cu-based methanol synthesis catalysts have not been clearly identified yet due to their complex nature and dynamic structural changes during reactions. Herein, atomically dispersed Zn on ZrO_2 support is established in Cu-based catalysts by separating Zn and Zr components from Cu (Cu-ZnZr) via the double-nozzle flame spray pyrolysis (DFSP) method. It exhibits superiority in methanol selectivity and yield compared to those with Cu-ZnO interface and isolated ZnO nanoparticles. Operando X-ray absorption spectroscopy (XAS) reveals that the atomically dispersed Zn species are induced during the reaction due to the strengthened Zn-Zr interaction. They can suppress formate decomposition to CO and decrease the H_2 dissociation energy, shifting the reaction to methanol production. This work enlightens the rational design of unique Zn species by regulating coordination environments and offers a new perspective for exploring complex interactions in multi-component catalysts.

Introduction

CO_2 hydrogenation to methanol becomes a promising environmental-friendly route for combatting CO_2 emissions by "green" hydrogen from excess volatile regenerative electricity[1]. Meanwhile, methanol can be widely applied as a hydrogen carrier or an intermediate for high-value-added chemicals[2]. Therefore, great efforts should be devoted to the development and application of this bright technology. Cu/ZnO-based catalysts with high performance and low cost have been extensively studied[2b, 3]. However, the "self-organization", "dynamics" or "reversible" nature of Zn species has led to different mechanistic models for the explanation of their structural changes, lacking a crucial insight into the structure-activity relationship.

Generally, ZnO is assumed to be a physical spacer for stabilizing active Cu species and promoting the adsorption of reaction intermediates[4]. Then, unique active sites have attracted much attention, such as defective Cu surface due to the lattice strain generated by ZnO coverage[5], CuZn alloy derived from ZnO reduction[6], Zn migration to Cu surface[7], as well as the Cu-ZnO interface from surface oxidation during reaction[8]. Moreover, the structure of ZnO layers over Cu nanoparticles is metastable and sensitive to environmental conditions[9]. Zinc formate has been observed as an intermediate for methanol formation[10]. Therefore, many disputes have been caused over the "real" nature of Zn species during reactions[3a, 11], considering their dynamic changes with conditions[12]. To make matters worse, the current results are based on different mechanistic models (such as ZnO_x[13], Cu/ZnO interface[14], ZnO coverage[15], CuZn alloy models[7b] or inverse ZnO/Cu[8a] catalyst), various reaction atmospheres (such as CO/H_2[7b], CO_2/H_2[8a] or $CO/CO_2/H_2$[5]) and different catalytic systems (such as Cu/ZnO[16], $Cu/ZnO/Al_2O_3$[5b, 15], $Cu/ZnO/SiO_2$[8b], Cu-Zn-Zr catalysts[17] or $ZnZrO_2$ solid solution[18]). Although ZnO-ZrO_2 interfaces were reported to be the active sites for CO_2 adsorption and conversion[18], Cu is necessary to facilitate H_2 dissociation[17]. The impact of the local structure or dispersion state of Zn species on those functional species is not mentioned. These leave many open questions about the nature of Zn species and their essential role in this highly relevant industrial reaction, especially when they are combined with other components. Therefore, the rational design of different structures of Zn species in one specific catalyst system with fixed components is required.

In this work, different Zn species were synthesized in a series of Cu-Zn-Zr ternary catalysts by separating one from the other two components *via* the double-nozzle flame spray pyrolysis (DFSP) method[19]. This method can combine two precursors of the three components in different orders to strengthen their interactions when they were in the same flame and meanwhile prevent the formation of composite in separate flames[20]. Thus, the controllable synthesis of comparable catalysts can be achieved, which is beneficial for making clear and direct connections between catalyst structure and reaction performance. Operando X-ray absorption spectroscopy (XAS) was used to unravel the local structure of Zn atoms and monitor the structural evolution of Zn species with varying conditions from reduction to reaction. In situ/operando diffuse reflectance infrared Fourier transform

spectroscopy (DRIFTS) was conducted for tracking the reaction intermediates at both low and high pressures. DFT calculations are devoted to the reaction mechanism analysis. These combined studies aimed to establish a persuasive relationship between the local structure of Zn species and their role in the CO_2 hydrogenation reaction, which will be beneficial in exploring complex interactions of multi-component catalysts.

Results and Discussion

Catalytic Performance

It is widely known that ZnO and ZrO_2 have their contributions to the catalytic performance of Cu-based catalysts. As shown in Figure S1, the lack of neither ZnO nor ZrO_2 will lead to a decrease in methanol yield. Therefore, it is crucial to establish a Cu-Zn-Zr ternary system with all contributions from each component and regulate one single variable with others being fixed. The DFSP method is an extended method of simple flame spray pyrolysis (FSP)[21] by utilizing two nozzles to separate different components, where two nozzles were placed at a distance of 10 cm with an angle of 60° between the two flames as shown in Figure 1(a)[22]. Three precursors of Cu, Zn and Zr were divided into two parts and introduced into two nozzles with different combinations. The nanoparticles were separately produced by each flame, gathered at the junction and finally collected by the filter on the top as described in the experimental section of supporting information (SI). Metal precursors in the same nozzle were sprayed and combusted with strong interactions and then mixed homogeneously with the compound from the other nozzle but with weaker interaction, resulting in different ternary oxide mixtures in the desired catalysts (Figure 1b). A catalyst with the same three components was additionally synthesized by single-nozzle FSP for comparison (CuZnZr). Each metal oxide in all obtained catalysts is close to the nominal composition with a ratio of CuO: ZnO: ZrO_2 = 2: 1: 7 from Table S1 and in the same crystal phase (Figure S2). Figure 1c shows that the methanol selectivity decreases in the following sequence: Cu-ZnZr > Zr-CuZn > Zn-CuZr > CuZnZr, revealing that the interactions between different components greatly affect the reaction pathways to methanol. However, the methanol yield of the CuZnZr sample obviously increases since the Cu dispersions of DFSP-made samples are sacrificed as listed in Table S1. Especially, the exposed Cu active sites are less in Cu-ZnZr sample than the others, which is limited by the double flames preparation method, where Cu nanoparticles are produced individually without any supports. Despite the lowest exposed Cu surface areas, the Cu-ZnZr sample exhibits excellent catalytic performance on both methanol selectivity and yield, indicating that the Zn species have a great contribution to methanol production. Noting that no deactivation can be observed during a 50-100 h test, even for the Cu-ZnZr catalyst with weak Cu-support interactions (Figure S3). In comparison, it showed higher methanol selectivity and yield normalized per Cu weight than the commercial $Cu/ZnO/Al_2O_3$ (see Figure S4 and Table S2). Given the same components in all samples, the controlling of Zn species via the combinations among multiple components during the DFSP process is effective, and the nature of Zn species is highly essential to methanol production.

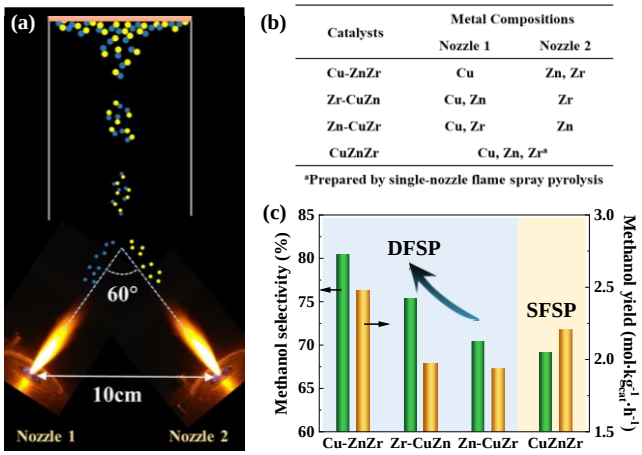

Figure 1. Catalysts design and catalytic performance. (a) Illustration of synthesis process by DFSP method; (b) Distribution of components in the two nozzles (DFSP) and the single-nozzle (SFSP); (c) Selectivity and space-time yield (STY) of methanol for different samples over CO_2 hydrogenation to methanol reaction. Reaction conditions: 220 °C, 3.0 MPa, CO_2:H_2 =1:3 and GHSV=6000 mL/(g_{cat}·h).

Morphological analysis

The morphology, distribution and crystal phase were characterized by transmission electron microscopy (TEM). Spherical nanoparticles with sizes of about 10-20 nm were observed for all samples (Figure S5). For Cu-ZnZr, ZnO lattice fringes could not be found from the Fast Fourier Transform analysis (FFT) of TEM images (Figure S6), and the energy-dispersive X-ray spectroscopy (EDS) mapping (Figure S7) exhibits that Zn species are well dispersed on the surface of ZrO_2 support. For Zr-CuZn, the t-ZrO_2 phase can be easily identified irrespective of the size of the particles (Figure S8). The close interaction of Cu and ZnO is found in the elemental mapping, where they always show up in the same area (Figure S9). Likewise, the separation of ZnO from the other components in the Zn-CuZr sample is observed in the TEM images and the elemental mapping (Figures S10 and S11, respectively).

Local structure analysis

To determine the effect of different interactions controlled by the DFSP process on the local structure of Cu and Zn species, the operando X-ray absorption spectroscopy (XAS) experiments were performed by using the high-pressure cell developed recently[23], which was applicable for XAS in transmission mode up to 50 bar and 450 °C. The experimental procedure is schematically represented in Figure S12. The Cu K-edge and Zn K-edge extended X-ray absorption fine structure (EXAFS) spectra up to k = 12 Å^{-1} were recorded at 50 °C on the as-prepared (I), reduced (III) and reacted (VI) samples. X-ray near-edge absorption (XANES) spectra up to k = 8 Å^{-1} were continuously collected with an interval of four minutes during the reduction (II), CO_2 adsorption (IV) and reaction (V) to track the changes in the chemical environment of Cu or Zn atoms.

Identification of Cu species. From the XANES spectra at Cu K-edge in Figure S13, the formation of a shoulder at 8980 eV and the decrease in white line intensity confirm that the local

structure of the Cu nanoparticles closely resembles the metallic copper and keeps stable in the reaction process without re-oxidation or carbonization for all samples. Therefore, the enhancement of methanol formation must be related to the property of the other components in those ternary oxides.

Identification of Zr species. As reported, the tetragonal phase of ZrO_2 support has a great impact on the catalytic performance due to the strong interaction with Cu[24], surface reaction[25] and the lower activation energy of methanol formation[26]. Here, the EXAFS spectra at Zr K-edge were measured for the as-prepared and reacted samples as shown in Figures S14 and S15. The crystal structure of Zr species in the as-prepared Cu-Zn-Zr ternary catalysts is close to the tetragonal ZrO_2 reference, which is consistent with XRD results. The valence states and the local structure of t-ZrO_2 for all samples remain unchanged during the reaction, excluding the effect of the ZrO_2 crystal phase on the catalytic performances.

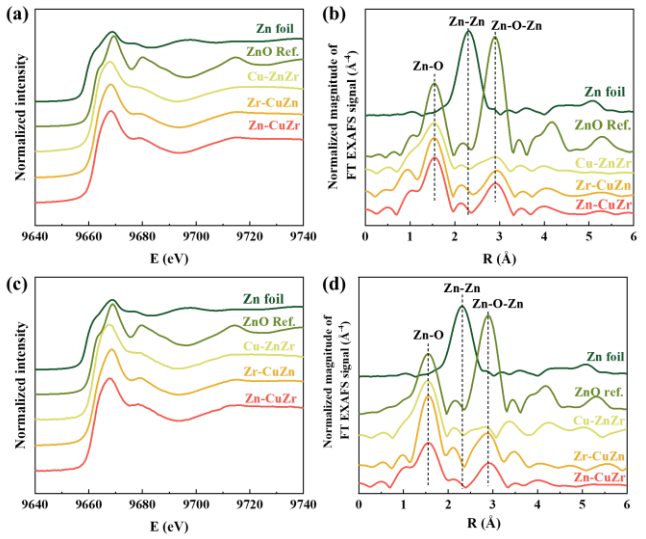

Figure 2. XAS spectra at Zn K-edge of all the as-prepared (a and b) and reacted (c and d) samples, compared with the standard spectra of Zn foil and ZnO reference, where (a) and (c) are normalized XANES spectra, and (b) and (d) are k^3-weighted FT EXAFS spectra.

Identification of Zn species. The absorption edge in the X-ray absorption near-edge structure (XANES) spectrum reveals that the Zn species are present in the +2 valence state in all the as-prepared samples since it is close to the 9662 eV characteristic for ZnO (Figure 2a). The discrepancy in the shape of the white line and the structure of the post-edge region in comparison with a tetragonal ZnO reference may indicate a modification of Zn oxides due to the interactions of ZnO with a second component or nano-structuring of ZnO[27]. From the analysis of the Fourier transformed k^3-weighted extended X-ray absorption fine structure (EXAFS) in Figure 2b, the first and the second shell scatterings at 1.6 and 2.9 Å without phase correction in all samples correspond to O and Zn neighbors as in ZnO, respectively. The number of Zn−O−Zn neighbors in the second coordination shell (peak at about 2.9 Å) is significantly less compared to the ZnO reference, indicating that a disorder of the atomic arrangement around the Zn atoms in ternary oxides is present. After the reaction, the Zn species in the Cu-ZnZr sample is significantly different from those in the other two catalysts through the observation of features in XANES spectra (Figure 2c) and the deformed shape from the second shell at a longer distance in EXAFS spectra (Figure 2d). For Zr-CuZn and Zn-CuZr catalysts, no obvious change in the intensity of the peaks can be observed compared to the as-prepared ones.

Tetragonal ZnO (ICSD 34477) with lattice constant a=b=3.253 Å and c=5.213 Å is used as a model for the fitting of EXAFS spectra[8b]. The EXAFS spectra at the Zn K-edge of all the as-prepared and reacted catalysts can be well-fitted as shown in Figure S16 and Table 1. As for as-prepared samples, the coordination numbers (CNs) of Zn−O in the first shell are close to 4, while those of Zn−O−Zn in the second shell are much smaller than ZnO. The CN of the Zn−O−Zn shell over the Cu-ZnZr is the lowest and close to 1, indicating it contains binuclear ZnO clusters. While for the other two samples, small ZnO nanoparticles with CN of Zn−O−Zn around 2-3 are formed during the DFSP process. This reveals that the interaction between Zn and other components will affect the ZnO particles, where the one without any interactions (Zn-CuZr) owns the largest ZnO. After the reaction, the Zn state is still in oxidation after CO_2 adsorption and reaction process, since CO_2 can stabilize the oxidation state even in the H_2 atmosphere[6]. It is found that the CNs of Zn−O for all three samples slightly decrease after the reaction. For the second shell, it is observed that the CN of Zn−O−Zn decreases from 1.2 to 0.5 for the Cu-ZnZr sample during the reaction, which is close to the reported value for the atomically dispersed Zn on ZrO_2 support or pseudo-single-atom structures[28], denoted as Zn_nO_x (n=1 or 2). Note that EXAFS is a short-range order analysis technique with very few coordination spheres. The dominant contribution to the static disorder that could show weaker EXAFS is from the surface atom bond relaxation of nanoscale clusters[29]. They should be located on the surface with the CN of the Zn–O shell around 3.5, otherwise, it would be coordinated by seven O atoms if they were in the bulk of tetragonal ZrO_2[30]. It reveals that the ZnO clusters are further dispersed during the reaction to form a Zn_nO_x-ZrO_2 atomic interface with the assistance of strong interaction with ZrO_2 support. It is attributed to the unstable and disordered ZnO structure with very low CN of Zn−O−Zn, as well as the intimate contact between Zn and Zr species in the as-prepared catalyst created by the FSP method. For Zr-CuZn and Zn-CuZr, the CNs of the Zn-O-Zn shell stay at the same level as those in the as-prepared samples. Although CuZn alloy is not detected, their interaction can be confirmed by high-pressure reaction as reported before[9b, 31], resulting in the formation of strong interaction on the Cu-ZnO interface[32]. The above analyses indicate that the structure of Zn species is very sensitive to their interactions with other components, especially with Zr. Therefore, the nature of Zn species can be tuned by the strong interaction created in the same flame and depends on the element of the second component, where Zr in Cu-ZnZr is more pronounced than Cu in Zr-CuZn catalysts.

Table 1. Fitting parameters resulting from analysis of Zn K-edge EXAFS collected at 50 °C for three as-prepared and reacted catalysts. Spectra of all samples were k^3-weighted and fitted in the range of R = 1.1-3.8 Å and k = 3.0-10.5 $Å^{-1}$. The amplitude reduction factor (S_0^2), as determined from Zn foil, was fixed at 0.967, and

one energy shift parameter (δE_0) was defined for all scattering paths. The coordination numbers (CN), the bond lengths (Distance), and Debye-Waller factors (σ^2) were fitted as guess parameters. Standard tetragonal ZnO model (ICSD34477): Zn−O with CN=4 at 1.98 Å, Zn−O−Zn with CN=12 at 3.23 Å.

Category	Sample	CN (Zn-O)	Zn-O Distance / Å	CN (Zn-O-Zn)	Zn-O-Zn Distance / Å	σ^2 / 10^{-3} Å^2	δE_0 / eV	R factor
Reference	ZnO	4	1.96±0.02	12	3.24±0.01	4.3±0.9	4.2±0.4	0.003
As-prepared	Cu-ZnZr	3.9±0.4	1.96±0.01	1.2±0.5	3.23±0.01	4.4±2.4	9.4±1.4	0.007
	Zr-CuZn	3.9±0.5	1.98±0.01	2.2±0.6	3.23±0.02	6.5±1.7	1.5±1.3	0.017
	Zn-CuZr	3.9±0.3	1.97±0.01	2.7±0.5	3.22±0.01	7.3±1.2	1.6±0.9	0.005
Reacted	Cu-ZnZr	3.5±0.4	1.97±0.01	0.5±0.3	3.21±0.04	3.7±1.6	1.7±1.3	0.019
	Zr-CuZn	3.8±0.6	1.98±0.02	2.9±1.1	3.23±0.02	8.0±2.6	2.4±1.8	0.024
	Zn-CuZr	3.2±0.4	1.97±0.01	2.8±0.5	3.24±0.02	3.5±1.6	2.0±1.5	0.022

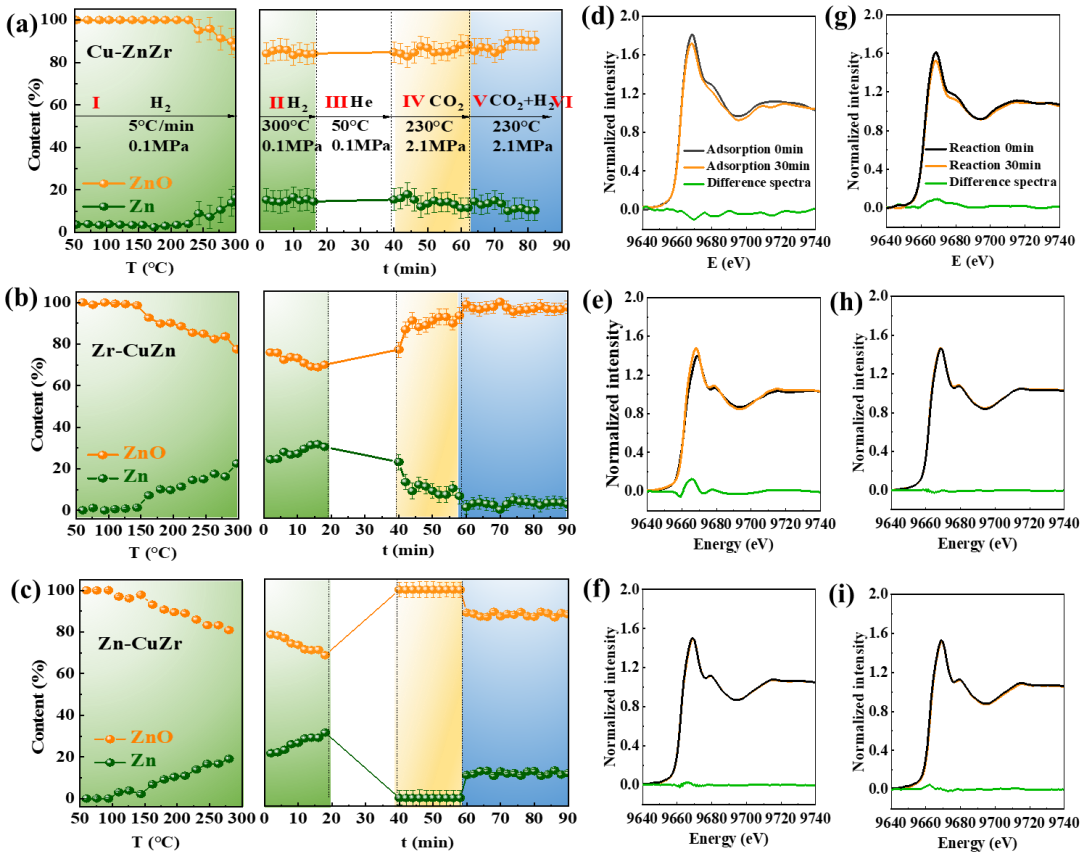

Figure 3. Variations of Zn chemical state analyzed by LCF according to the XANES spectra that were obtained during a successive in situ XAS experiment (Figure S12) over (a) Cu-ZnZr, (b) Zr-CuZn and (c) Zn-CuZr samples, where the first scan spectra (denoted as ZnO) and Zn foil were used as standards. Normalized XANES spectra at Zn K-edge during 30 min CO_2 adsorption (d, e, f) and 30 min CO_2 hydrogenation reaction (g, h, i) over Cu-ZnZr (d, g), Zr-CuZn (e, h) and Zn-CuZr (f, i) samples. The difference spectra between those at 0 min (black line) and 30 min (orange line) are plotted as green lines.

Dynamic behavior of Zn species. The structural changes of Zn species under different conditions (gas atmosphere, temperature and pressure) were successively monitored according to the reaction protocol described in Figure S12 by

operando XAS at the Zn K-edge[12]. After reduction, ZnO was partly reduced, seen as a characteristic change in the shape of the XANES spectra (Figure S17a). The XANES feature became broader and a shoulder at 9663 eV appeared. The feature at 9680 eV of the metallic Zn increased, while the white line intensity of ZnO spectra decreased. It is worth noting that no characteristic feature of Cu-Zn alloy in the brass model at 9700 eV[12] can be observed for any of the three samples, demonstrating the absence of Cu-Zn alloy in the DFSP-made samples during the reduction at 300 °C even in the case of intimate contact between Cu and Zn (Zr-CuZn sample). In FT-EXAFS spectra (Figure S17b), the peak belonging to the Zn−O path in the first shell becomes broader, containing both the Zn−O bond and a contribution of Zn−Zn interaction. Moreover, the chemical state of Zn species is analyzed by linear combination fitting (LCF) according to the XANES spectra obtained during the operating conditions in Figure 3(a, b, c). The variations of XANES spectra during the reduction process and the fitting results are shown in Figure S18. For Cu-ZnZr, the ZnO starts to be reduced at about 240 °C. Less than 20 % ZnO is reduced at 300 °C, and the Zn chemical state is observed to remain almost stable during the subsequent process, proving the formation of a stable structure. In comparison, the ZnO is easier to be reduced at a relatively low reduction temperature (150 °C) for both Zr-CuZn and Zn-CuZr samples. Subsequently, the Zn species in Zr-CuZn are gradually oxidized in the CO_2 atmosphere and remain stable even after introducing hydrogen. However, for Zn-CuZr, the oxidation happens in CO_2 in a short time and further increases in the reaction atmosphere, revealing that the Zn valence state is susceptible to the gas atmosphere. The structural evolution of Zn under the reaction atmosphere (CO_2 or CO_2+H_2) was evaluated by the comparison of the XANES spectra at the beginning (0 min) and the end (30 min) of the CO_2 adsorption or CO_2 hydrogenation reaction at 2.1 MPa in Figures 3(d-i). Significant changes in the pre-edge features rather than energy shifts are observed over the Cu-ZnZr sample in both CO_2 and CO_2+H_2 atmosphere, indicating that the structure of Zn species is very sensitive to chemical environments. The changes cannot be explained by oxidation or reduction without energy shifts but may belong to the configuration or coordination environment of Zn atoms from the deformed spectra. In contrast, the Zn species in the Zn-CuZr sample seems to be stable during the whole process, acting as a spectator. For Zr-CuZn, the changes can be only detected in the CO_2 adsorption process in the edge region, revealing that the Zn species is re-oxidized by CO_2. This phenomenon is consistent with the LCF results.

During XANES experiments under reaction conditions, the outlet gas was analyzed by online gas chromatography to evaluate the relationship between Zn species and the catalytic performance. Cu-ZnZr catalyst exhibited the highest activity in methanol production (34.3 mmol/g_{cat}·h), while those of Zr-CuZn and Zn-CuZr were 24.7 and 17.5 mmol/g_{cat}·h, respectively. These results are in agreement with the catalytic performance tested in the laboratory with a fixed-bed reactor.

Analysis of reaction intermediates

For the CO_2 hydrogenation to methanol over Cu-based catalysts, formate (*HCOO) is produced by the reaction between adsorbed CO_2 and dissociated H, and its further hydrogenation to methoxy (CH_3O*), which subsequently leads to methanol formation[33]. The evolution of the key intermediates (formate and methoxy) for each reduced catalyst is monitored by in situ DRIFTS at atmospheric pressure. The spectra are shown in Figure 4, and the assignments of peaks are listed in Table S3. For clear understanding, the features at 2930 and 2878 cm^{-1} are normalized by the peak area at the end of the reaction, representing the variation of the two main intermediates (formate and methoxy, respectively). Usually, formate hydrogenation to methoxy requires a high energy barrier, leading to the delayed and weak generation of methoxy on the surface. Here, an accumulation of formate is observed during the reaction period for all three samples, but methoxy can only be formed on Cu-ZnZr and Zr-CuZn rather than Zn-CuZr, indicating that the transformation from formate to methoxy on Zn-CuZr is obstructed. When switching to the He atmosphere, methoxy species quickly decrease due to the desorption of unstable intermediates for both Cu-ZnZr and Zr-CuZn catalysts. However, the formate species are slightly increased and remain stable on Cu-ZnZr but gradually decrease on Zr-CuZn, revealing that the adsorption of formate is stronger on the former than the latter during the CO_2 hydrogenation. Weakly adsorbed formate intermediates cannot further hydrogenate to methoxy and methanol due to its decomposition into gaseous CO on the FSP-made ZrO_2 support, while strong adsorption on the ZnO_x-ZrO_2 atomic interface will inhibit the formate decomposition at reaction temperature (below 250 °C) as observed in HCOOH temperature program desorption (HCOOH-TPD) in Figure S19. The adsorbed HCOO* on ZrO_2 support will dehydrate into CO during a wide range from 150-400 °C without detection of CO_2, while HCOO* can be hydrogenated and decomposed into CO_2 by surface dissociated H* that is activated by ZnO site[34] at about 250-300 °C for Zn modified ZrO_2 support.

Although the signals observed by in situ DRIFTS at atmospheric pressure can give more information on the intermediates' adsorption or desorption properties for different catalysts, those at high pressure reflect the reality that happened at the operating reaction conditions[35]. The intermediates consumption and the product generation were monitored during DRIFTS experiments at reaction pressure (3.0 MPa) as shown in Figure 5, reflecting the catalytic performance of catalysts. The vibrational frequencies are much weaker at high pressure than those at atmospheric pressure since the conversion of intermediates to the product is enhanced. For Cu-ZnZr, the formate features at 2878 and 1620 cm^{-1} are weakened and those among 1300-1500 cm^{-1} are barely observed, while methoxy at 2936 cm^{-1} is enhanced compared to the other two samples, revealing that the successive hydrogenation process is accelerated[5b]. However, for Zr-CuZn and Zn-CuZr, formate remains on the catalyst, while the feature of methoxy is almost absent. Moreover, the residue formate species are higher for Zn-CuZr than Zr-CuZn, which is attributed to the absence of active hydrogen for the hydrogenation reaction to methoxy and methanol products. The unconverted formate at high pressure benefits the dehydration reaction to the by-product CO at 2094, 2077 and 2053 cm^{-1} as observed before[36]. The catalytic performance, especially for the methanol selectivity, can be well related to the adsorption behavior of intermediates which can be adjusted by the structure of Zn species formed in the three catalysts

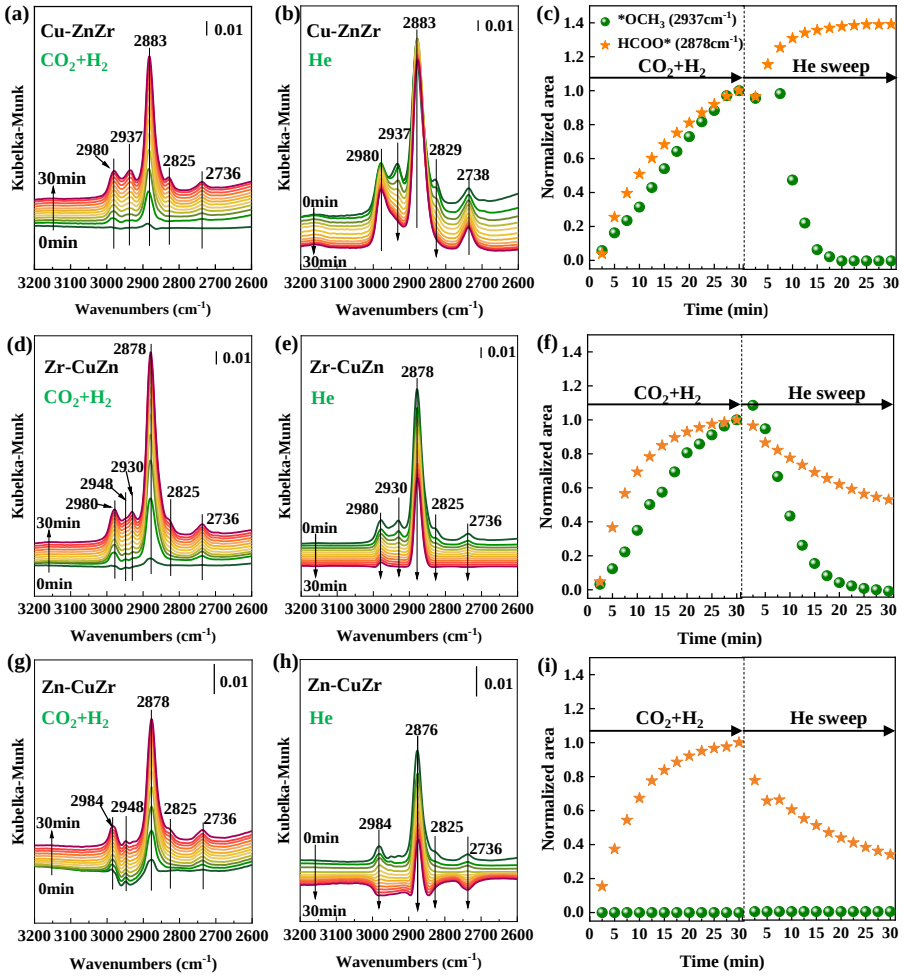

Figure 4. In situ DRIFTS spectra of (a, b, c) Cu-ZnZr, (d, e, f) Zr-CuZn and (g, h, i) Zn-CuZr catalysts during CO_2 hydrogenation (a, d, g) reaction followed by He sweep after reaction (b, e, h). Reaction conditions: 0.1 MPa, 230 °C, 50 mL/min, CO_2:H_2=1:3. The evolution of normalized peak area of formate HCOO* (2878 cm^{-1}, orange) and methoxy *OCH_3 (2936 cm^{-1}, green) for (c) Cu-ZnZr, (f) Zr-CuZn and (i) Zn-CuZr catalysts.

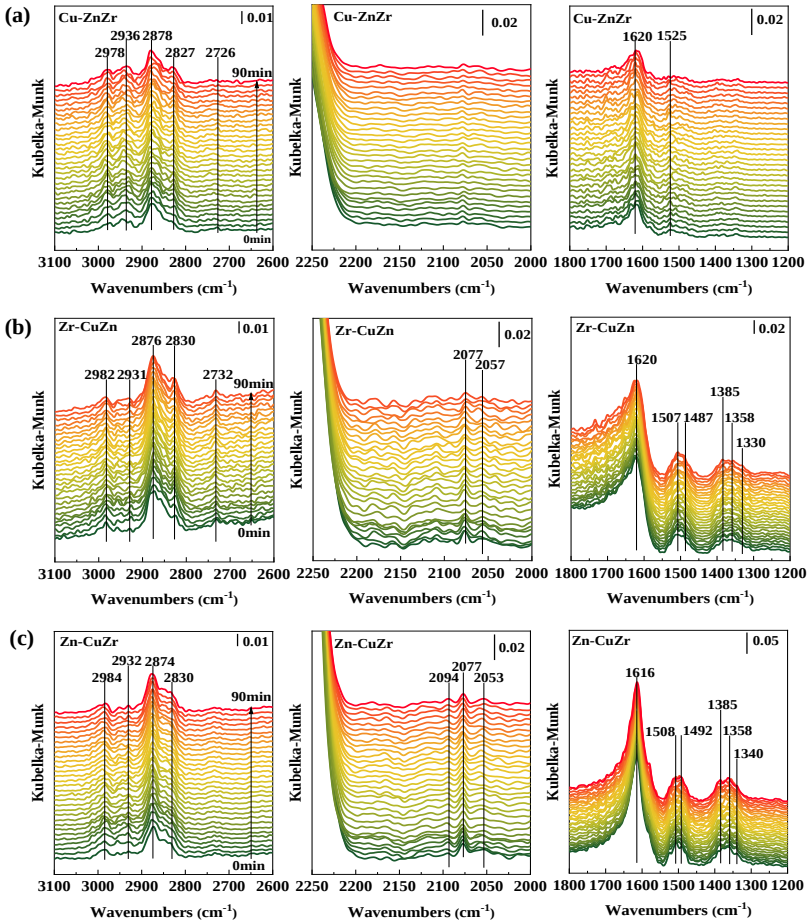

Figure 5. Operando DRIFTS spectra of (a) Cu-ZnZr, (b) Zr-CuZn and (c) Zn-CuZr in the process of CO_2 hydrogenation at elevated pressure. Reaction conditions: 3.0 MPa, 230 °C, 50 mL/min, CO_2: H_2=1: 3.

Analysis of hydrogen activation

During the CO_2 hydrogenation reaction, hydrogen activation is important in the tandem hydrogenation of CO_2 to formate intermediates and finally to methanol. From H_2-TPD in Figure S20, active hydrogen for the hydrogenation from formate to methoxy can be created on the Cu-Zn interface over Cu-ZnZr and Zr-CuZn catalysts, but hard to be obtained in Zn-CuZr due to the separation of Cu and Zn. Although ZnO-ZrO_2 compounds synthesized by SFSP had a positive function in H_2 activation compared to that of independent ZnO and ZrO_2 oxides, Zn species have fewer contributions without interacting with Cu. Thus, H_2-D_2 isotopic exchange experiments were conducted for quantitative analysis of active hydrogen on the Cu-Zn interface (see Figure S21). It shows that the catalysts without Cu or Zn are weakened in H_2 activation. The capability of H/D exchange is higher for Cu-ZnZr than that for Zr-CuZn, revealing that the interface between Cu and different Zn species or both Cu and Zn sites are crucial for hydrogenation[17].

To gain further insights at a molecule level, DFT calculation was employed to estimate the energy barrier in H_2 activation on the interface between Cu and atomically dispersed Zn in ZrO_2 support (Model 1) as well as the Cu-ZnO interface (Model 2), described in Figure S22, according to the structure analysis from the above experimental results in Cu-ZnZr and Zr-CuZn samples, respectively. As shown in Figure 6 and Table S4, both adsorption and dissociation paths with energy differences of -0.097 and -0.425 eV, respectively, on the Zn sites in Model 1 are weaker than those on the Zn sites in Model 2. However, the activation energy for transition states (TS) formation is a determining factor to estimate the whole process. It is much lower in Model 1 (0.148 eV) than that in Model 2 (0.477 eV), suggesting that H_2 activation is more thermodynamically favorable on the Cu-ZnZr catalyst. It demonstrates that the unique structure of atomically dispersed Zn in ZrO_2 support facilitates the reduction of the energy barrier in the key step of H_2 activation, and probably accelerates the hydrogenation of adsorbed intermediates to methanol. Furthermore, DFT calculation of H_2 activation on different sites in Model 1 was also conducted, including the surface of metallic Cu sites, atomically dispersed Zn sites and Zr sites on the surface of ZrO_2 support, as shown in Figure S23. Both adsorption and dissociation energy at Zr sites are positive values, suggesting that the H_2 molecule is very difficult to be activated. In comparison, the H_2 activation prefers occurring at Cu and Zn sites due to the negative energy differences. The activation energy of the former (0.542 eV) is obviously higher than that of the latter (0.148 eV).

These findings suggest that the H_2 activation on the Cu-ZnZr catalyst is more preferential at the atomically dispersed Zn sites than the Cu sites, but barely occurs on Zr sites. Dual-site activation of H_2 from both Cu and Zn contributes to the reaction from different hydrogenation steps[37]. The Zn function in the hydrogenation process is strengthened by the establishment of unique atomically dispersed Zn sites in Cu-based catalysts.

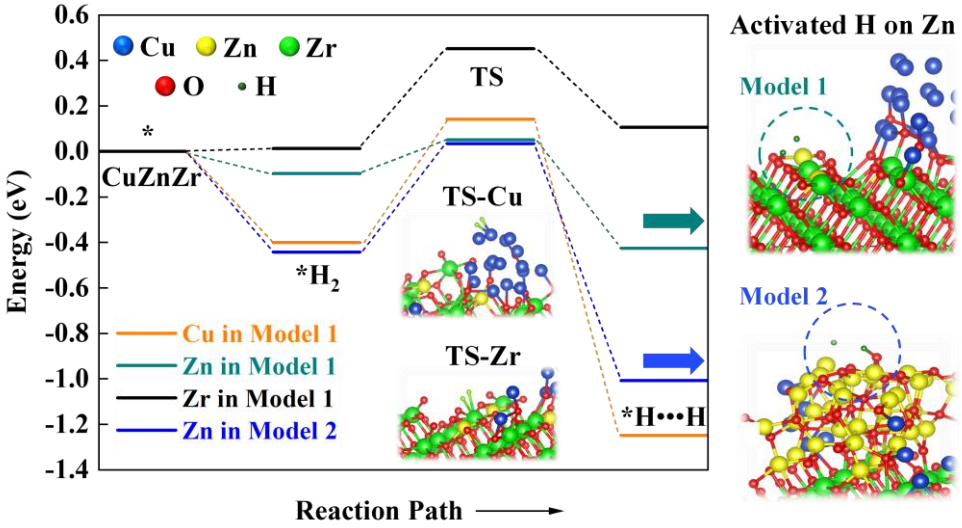

Figure 6. DFT calculation of H_2 dissociation on Cu, Zn and Zr sites in Model 1, as well as on Zn sites in Model 2 in Cu-Zn-Zr ternary catalysts. Models 1 and 2 represent the interface between Cu and atomically dispersed Zn on ZrO_2 support in the Cu-ZnZr sample and the Cu-ZnO interface in the Zr-CuZn sample, respectively. The descriptions of models and different sites were shown in Figures S22 and S23, respectively.

Analysis of the reaction mechanism

It is widely accepted that methanol synthesis over Cu-Zn-Zr ternary catalysts follows the formate pathway, reflecting that the chemisorption properties of formate species and the successive hydrogenation steps on the catalyst surface have a significant effect on the following selective conversion to methoxy and methanol due to higher energy barrier for hydrogenation[38] than that for the decomposition into by-product CO[36]. Based on the results obtained in this work, the catalysts with different Zn species produced by DFSP have a great effect on this reaction process as shown in Figure 7. It can be proposed that H_2 is activated and dissociated on the interface between Cu and Zn species. CO_2 is first hydrogenated into formate species and then further to methoxy and methanol, where the intermediate formate species can also decompose into CO in the case of weak adsorption or weak hydrogenation. The enhancement of successive hydrogenation of formate to methoxy and methanol rather than decomposition to CO can be attributed to the strengthened formate adsorption and the lower hydrogen activation energy to supply more active H species on the unique Cu-Zn_nO_x atomic interface in Cu-ZnZr catalyst. For the Zr-CuZn catalyst, the hydrogen dissociation is also enhanced by the strong Cu-ZnO interaction owing to the combination of Cu and Zn precursors in one nozzle compared to that on Cu sites, however, weak formate adsorption is disadvantageous to the methanol production. Even worse, the hydrogen dissociation is suppressed without Zn promotion when Zn is acting as a spectator in the form of isolated ZnO species in the Zn-CuZr catalyst, leading to the lowest methanol selectivity. In this work, we demonstrate that the structure of active Zn species has a great effect on the intermediate adsorption and conversion.

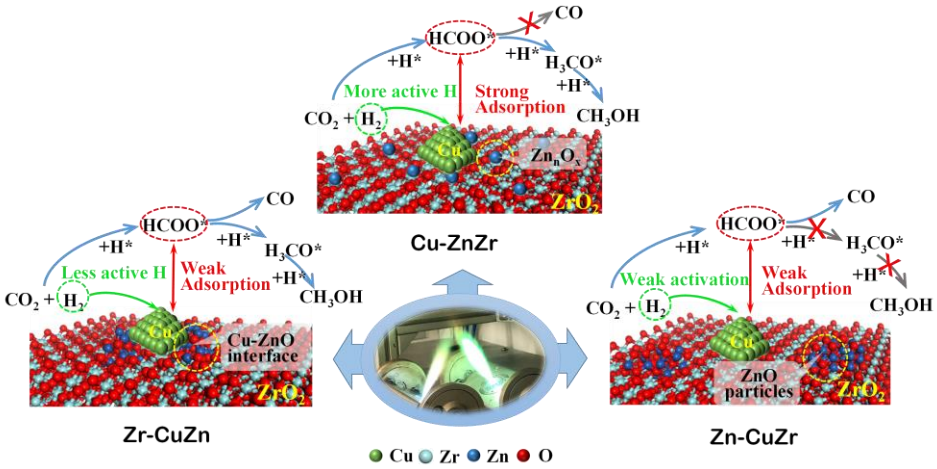

Figure 7. The proposed reaction mechanism of CO_2 hydrogenation to methanol over Cu-Zn-Zr ternary catalysts produced by the DFSP method.

Conclusion

For a highly demanding CO_2 to methanol conversion, a series of Cu-Zn-Zr ternary catalysts with fixed components but different Zn local structures were controllably synthesized by strengthening the Cu-Zn or Zn-Zr interactions *via* the DFSP method. These catalysts exhibit distinct methanol selectivity and yield in the following sequence: Cu-ZnZr > Zr-CuZn > Zn-CuZr. Dynamic structural evolution of Zn species analyzed by operando XAS shows that atomically dispersed Zn sites are created at reaction conditions due to the strong interaction between the highly dispersed ZnO clusters and ZrO_2 support in the initial state of the Cu-ZnZr catalyst. The in situ and operando DRIFTS experiments as well as DFT calculations reveal that this unique Zn species promotes the selective conversion to methoxy and subsequently to methanol rather than decomposition to CO owing to the strengthened formate adsorption and the low hydrogen activation energy. This exceeds the function of the generally-accepted active Cu-ZnO interface of the Zr-CuZn catalyst in promoting methanol production. In comparison, the relatively large and independent ZnO nanoparticles on the Zn-CuZr catalyst have the least contribution due to the lack of promotion on both hydrogen activation and formate stabilization. The results reveal that the methanol synthesis on Cu-based catalysts strongly depends on the structure of Zn species, which can be easily controlled by the interaction with other components in preparation, exhibiting high potential in the design of effective species in multi-component catalysts.

Acknowledgments

This study is supported by the Natural Science Foundation of China (Grant 22172169). We would like to thank the Institute for Beam Physics and Technology (IBPT-KIT) for the operation of the storage ring, the Karlsruhe Research Accelerator (KARA). We acknowledge the KIT light source for the provision of instruments at the CAT-ACT beamline of the Institute of Catalysis Research and Technology (IKFT-KIT). We are grateful to Dr. Alexey Boubnov for his help during the beamtime and his expertise in XAS and data analysis. Dr. Yu greatly acknowledges the visiting scholarship from the Chinese Academy of Sciences.

Keywords: CO_2 hydrogenation• Methanol synthesis• Flame spray pyrolysis• Cu catalysts• X-ray absorption spectroscopy

[1] a) G. A. Olah, *Angew. Chem., Int. Ed.* **2005**, *44*, 2636-2639; b) J. Wei, R. Yao, Y. Han, Q. Ge, J. Sun, *Chem. Soc. Rev.* **2021**, *50*, 10764-10805; c) K. F. Kalz, R. Kraehnert, M. Dvoyashkin, R. Dittmeyer, R. Gläser, U. Krewer, K. Reuter, J.-D. Grunwaldt, *ChemCatChem* **2017**, *9*, 17-29.

[2] a) C. F. Shih, T. Zhang, J. Li, C. Bai, *Joule* **2018**, *2*, 1925-1949; b) J. Zhong, X. Yang, Z. Wu, B. Liang, Y. Huang, T. Zhang, *Chem. Soc. Rev.* **2021**, *49*, 1385-1413.

[3] a) S. R. Docherty, C. Copéret, *J. Am. Chem. Soc.* **2021**, *143*, 6767-6780; b) M. Behrens, *Angew. Chem. Int. Ed.* **2014**, *53*, 12022-12024.

[4] M. Behrens, *J. Catal.* **2009**, *267*, 24-29.

[5] a) I. Kasatkin, P. Kurr, B. Kniep, A. Trunschke, R. Schlogl, *Angew. Chem., Int. Ed.* **2007**, *46*, 7324-7327; b) M. Behrens, F. Studt, I. Kasatkin, S. Kühl, M. Hävecker, F. Abild-Pedersen, S. Zander, F. Girgsdies, P. Kurr, B.-L. Kniep, M. Tovar, R. W. Fischer, J. K. Nørskov, R. Schlögl, *Science* **2012**, *336*, 893-897.

[6] P. Amann, B. Klötzer, D. Degerman, N. Köpfle, T. Götsch, P. Lömker, C. Rameshan, K. Ploner, D. Bikaljevic, H.-Y. Wang, M. Soldemo, M. Shipilin, C. M. Goodwin, J. Gladh, J. Halldin Stenlid, M. Börner, C. Schlueter, A. Nilsson, *Science* **2022**, *376*, 603-608.

[7] a) R. van den Berg, G. Prieto, G. Korpershoek, L. I. van der Wal, A. J. van Bunningen, S. Laegsgaard-Jorgensen, P. E. de

Jongh, K. P. de Jong, *Nat. Commun.* **2016**, *7*, 13057; b) D. Grandjean, V. Pelipenko, E. D. Batyrev, J. C. van den Heuvel, A. A. Khassin, T. M. Yurieva, B. M. Weckhuysen, *J. Phys. Chem. C* **2011**, *115*, 20175-20191.

[8] a) S. Kattel, P. J. Ramírez, J. G. Chen, J. A. Rodriguez, P. Liu, *Science* **2017**, *355*, 1296-1299; b) N. J. Divins, D. Kordus, J. Timoshenko, I. Sinev, I. Zegkinoglou, A. Bergmann, S. W. Chee, S. Widrinna, O. Karslioglu, H. Mistry, M. Lopez Luna, J. Q. Zhong, A. S. Hoffman, A. Boubnov, J. A. Boscoboinik, M. Heggen, R. E. Dunin-Borkowski, S. R. Bare, B. R. Cuenya, *Nat. Commun.* **2021**, *12*, 1435-1445.

[9] a) T. Lunkenbein, J. Schumann, M. Behrens, R. Schlogl, M. G. Willinger, *Angew. Chem., Int. Ed.* **2015**, *54*, 4544-4548; b) J.-D. Grunwaldt, A. M. Molenbroek, N. Y. Topsøe, H. Topsøe, B. S. Clausen, *J. Catal.* **2000**, *194*, 452-460.

[10] M. Zabilskiy, V. L. Sushkevich, D. Palagin, M. A. Newton, F. Krumeich, J. A. van Bokhoven, *Nat. Commun.* **2020**, *11*, 2409.

[11] X. Jiang, X. Nie, X. Guo, C. Song, J. G. Chen, *Chem. Rev.* **2020**, *120*, 7984-8034.

[12] L. Pandit, A. Boubnov, G. Behrendt, B. Mockenhaupt, C. Chowdhury, J. Jelic, A.-L. Hansen, E. Saraçi, E.-J. Ras, M. Behrens, F. Studt, J.-D. Grunwaldt, *ChemCatChem* **2021**, *13*, 4120-4132.

[13] X. Liu, J. Luo, H. Wang, L. Huang, S. Wang, S. Li, Z. Sun, F. Sun, Z. Jiang, S. Wei, W.-X. Li, J. Lu, *Angew. Chem. Int. Ed.* **2022**, e202202330.

[14] S. Kuld, M. Thorhauge, H. Falsig, C. F. Elkjær, S. Helveg, Chorkendorff, J. Sehested1, *Science* **2016**, *352*, 969-974.

[15] A. Beck, M. Zabilskiy, M. A. Newton, O. Safonova, M. G. Willinger, J. A. van Bokhoven, *Nature Catal.* **2021**, *4*, 488-497.

[16] S. Kattel, P. J. Ramírez, J. G. Chen, J. A. Rodriguez, P. Liu, *Science* **2017**, *355*, 1296–1299

[17] Y. Wang, S. Kattel, W. Gao, K. Li, P. Liu, J. G. Chen, H. Wang, *Nat. Commun.* **2019**, *10*, 1166-1176.

[18] J. Wang, G. Li, Z. Li, C. Tang, Z. Feng, H. An, H. Liu, T. Liu, C. Li, *Sci. Adv.* **2017**, *3*, e1701290.

[19] a) T. Tran-Phu, R. Daiyan, X. M. C. Ta, R. Amal, A. Tricoli, *Adv. Funct. Mater.* **2022**, *32*, 2110020; b) S. Tada, K. Larmier, R. Büchel, C. Copéret, *Catal. Sci. Technol.* **2018**, *8*, 2056-2060.

[20] a) M. Tepluchin, D. K. Pham, M. Casapu, L. Mädler, S. Kureti, J.-D. Grunwaldt, *Catal. Sci. Technol.* **2015**, *5*, 455-464; b) M. Høj, D. K. Pham, M. Brorson, L. Mädler, A. D. Jensen, J.-D. Grunwaldt, *Catal. Lett.* **2013**, *143*, 386-394.

[21] a) R. Strobel, S. E. Pratsinis, *J. Mater. Chem.* **2007**, *17*, 4743-4756; b) R. Koirala, S. E. Pratsinis, A. Baiker, *Chem. Soc. Rev.* **2016**, *45*, 3053-3068.

[22] A. M. Gänzler, M. Casapu, F. Maurer, H. Störmer, D. Gerthsen, G. Ferré, P. Vernoux, B. Bornmann, R. Frahm, V. Murzin, M. Nachtegaal, M. Votsmeier, J.-D. Grunwaldt, *ACS Catal.* **2018**, *8*, 4800-4811.

[23] L. Pandit, M.-A. Serrer, E. Saraçi, A. Boubnov, J.-D. Grunwaldt, *Chemistry–Methods* **2022**, *2*, e202100078.

[24] M. Yang, J. Yu, X. Tong, X. Sun, H. Xu, J. Sun, *Chem. Commun.* **2021**, *57*, 7509-7512.

[25] F. C. F. Marcos, J. M. Assaf, R. Giudici, E. M. Assaf, *Appl. Surf. Sci.* **2019**, *496*, 143671.

[26] F. C. F. Marcos, F. M. Cavalcanti, D. D. Petrolini, L. Lin, L. E. Betancourt, S. D. Senanayake, J. e. A. Rodriguez, R. G. Jos´e M. Assafd, E. M. Assafb, *Chem. Eng. J.* **2022**, *427*, 130947.

[27] M. W. E. van den Berg, S. Polarz, O. P. Tkachenko, K. Kähler, M. Muhler, W. Grünert, *Catal. Letters* **2008**, *128*, 49-56.

[28] a) H. Wei, X. Liu, A. Wang, L. Zhang, B. Qiao, X. Yang, Y. Huang, S. Miao, J. Liu, T. Zhang, *Nat. Commun.* **2014**, *5*, 5634; b) X. Liu, J. Luo, H. Wang, L. Huang, S. Wang, S. Li, Z. Sun, F. Sun, Z. Jiang, S. Wei, W.-X. Li, J. Lu, *Angew. Chem. Int. Ed.* **2022**, *61*, e202202330; c) D. Zhao, X. Tian, D. E. Doronkin, S. Han, V. A. Kondratenko, J.-D. Grunwaldt, A. Perechodjuk, T. H. Vuong, J. Rabeah, R. Eckelt, U. Rodemerck, D. Linke, G. Jiang, H. Jiao, E. V. Kondratenko, *Nature* **2021**, *599*, 234-238.

[29] a) A. I. Frenkel, C. W. Hills, R. G. Nuzzo, *The Journal of Physical Chemistry B* **2001**, *105*, 12689-12703; b) B. B. Sarma, F. Maurer, D. E. Doronkin, J.-D. Grunwaldt, *Chem. Rev.* **2022**.

[30] S. Han, D. Zhao, T. Otroshchenko, H. Lund, U. Bentrup, V. A. Kondratenko, N. Rockstroh, S. Bartling, D. E. Doronkin, J.-D. Grunwaldt, U. Rodemerck, D. Linke, M. Gao, G. Jiang, E. V. Kondratenko, *ACS Catal.* **2020**, *10*, 8933-8949.

[31] J. Nakamuraa, Y. Choia, T. Fujitanib, *Top. Catal.* **2003**, *22*, 277-285.

[32] R. Naumann d'Alnoncourt, X. Xia, J. Strunk, E. Loffler, O. Hinrichsen, M. Muhler, *Phys. Chem. Chem. Phys.* **2006**, *8*, 1525-1538.

[33] Y. Wang, W. Gao, K. Li, Y. Zheng, Z. Xie, W. Na, J. G. Chen, H. Wang, *Chem* **2020**, *6*, 419-430.

[34] T.-y. Chen, C. Cao, T.-b. Chen, X. Ding, H. Huang, L. Shen, X. Cao, M. Zhu, J. Xu, J. Gao, Y.-F. Han, *ACS Catal.* **2019**, *9*, 8785-8797.

[35] K. Larmier, W.-C. Liao, S. Tada, E. Lam, R. Verel, A. Bansode, A. Urakawa, A. Comas-Vives, C. Copéret, *Angew. Chem. Int. Ed.* **2017**, *56*, 2318-2323.

[36] S. Kattel, B. Yan, Y. Yang, J. G. Chen, P. Liu, *J. Am. Chem. Soc.* **2016**, *138*, 12440-12450.

[37] L. Song, H. Wang, S. Wang, Z. Qu, *Appl. Catal. B: Environ.* **2023**, *322*, 122137.

[38] T. Liu, X. Hong, G. Liu, *ACS Catal.* **2019**, *10*, 93-102.

Entry for the Table of Contents

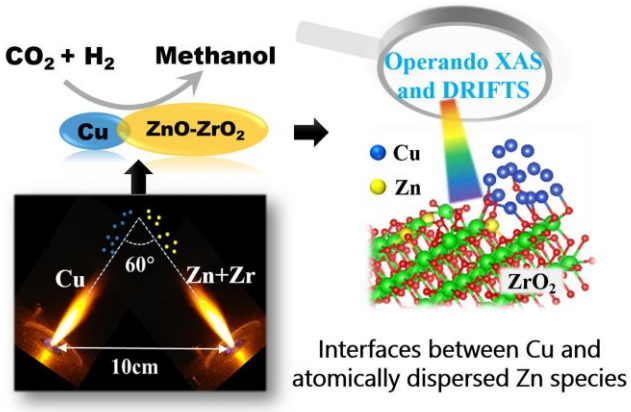

In Cu-Zn-Zr catalysts, interfaces between Cu and atomically dispersed Zn species are established by separating Zn and Zr from Cu in the two nozzles utilized during flame spray pyrolysis (FSP). Operando spectroscopies confirm that the structure is created during CO_2 hydrogenation, and it boosts methanol production by suppressing formate decomposition to CO and decreasing the H_2 dissociation energy.

Supporting Information for

Probing the Nature of Zinc in Copper-Zinc-Zirconium Catalysts by Operando Spectroscopies for CO_2 Hydrogenation to Methanol

Meng Yang[a,b], Jiafeng Yu[a,*], Anna Zimina[c,d], Bidyut Bikash Sarma[c,d], Lakshmi Pandit[c,d], Jan-Dierk Grunwaldt[d,c,*], Ling Zhang[a,b], Hengyong Xu[a], Jian Sun[a,*]

[a]Dalian Institute of Chemical Physics, Chinese Academy of Sciences, Dalian 116023, Liaoning, China
[b]University of Chinese Academy of Sciences, Beijing 100049, China
[c]Institute of Catalysis Research and Technology, Karlsruhe Institute of Technology, 76344 Eggenstein-Leopoldshafen, Germany
[d]Institute for Chemical Technology and Polymer Chemistry, Karlsruhe Institute of Technology, 76131 Engesserstraße 20, Karlsruhe, Germany

*Corresponding authors. E-mail addresses: yujf@dicp.ac.cn (Jiafeng Yu); grunwaldt@kit.edu (Jan-Dierk Grunwaldt); sunj@dicp.ac.cn (Jian Sun)

Experimental section

Catalysts preparation methods

The preparation of CuZnZr ternary catalysts by double-nozzle flame spray pyrolosis (DFSP) method were conducted in a double-nozzle FSP setup consisting of two conventional FSP nozzles as described elsewhere[1]. The two nozzles were positioned at an angle of 120° and a distance of 10 cm, resulting that the angle between the two flames being 60° as shown in Figure 1a and Figure S24a. The precursors of Cu, Zn and Zr were cupric acetate monohydrate (99.9%, Alfa Aesar), zinc acetate dihydrate (99.9%, Fluka) and zirconium oxide 2-ethylhexanoate in mineral oil (6 wt% Zr, Sigma-Aldrich), respectively. The proper amount of precursors was chosen resulting in a CuO: ZnO: ZrO_2 weight ratio of 2: 1: 7 in the prepared samples. Cu precursor was dissolved in the mixture of 2-ethylhexanonic acid (Sigma-Aldrich, analytical purity) and methanol (Sigma-Aldrich, analytical purity) solvent with the assistance of ultrasonic treatment. Zn precursor was dissolved in methanol, while the Zr precursor was liquid. For each sample, one component was separated from the other two, and they were separately injected into two individual FSP nozzles at a rate of 5 mL/min using a syringe pump (World Precision Instruments). Each spray was ignited by an annular premixed CH_4 flame (1.6 L/min of O_2 and 750 mL/min of CH_4). Oxygen was used as dispersion gas (5 L/min) at a 0.3 MPa pressure drop. The gas flows were controlled by mass flow controllers (Bronkhorst). The resulting particles were collected on glass fiber filters (24 cm diameter, Whatman GF6) in a water-cooled round holder connected to a vacuum pump (Busch R5). Herein, the as-prepared catalysts were named as Cu-ZnZr, Zr-CuZn and Zn-CuZr, where hyphen separated the components in two nozzles.

A CuZnZr ternary catalyst was also prepared by single-nozzle flame spray pyrolosis (SFSP) method, serving as a comparison material to show the effects of interactions between each two components. SFSP equipment is the same as DFSP but using one flame generator[2]. All precursors were dissolved in a mixture of 2-ethylhexanonic acid and methanol solvent (volume ratio was 4) and well mixed during the ultrasonic treatment. Then the solution was injected into the nozzle with a vertical flame to produce nanoparticles (Figure S24b), denoted as CuZnZr.

Oxides (ZnO, ZrO_2 and ZnO-ZrO_2) as well as catalysts with different components (Cu-Zn/ZrO_2, Cu/ZrO_2 and Cu-Zn/SiO_2) were prepared by SFSP. Tetraethyl orthosilicate (Aladin, Analytical Purity) was used as the Si precursor. Commercial Cu/ZnO/Al_2O_3 (CuZnAl) catalyst was purchased from ALLY HI-TECH Corporation.

Catalytic performance evaluation

The activity test was performed in a high-pressure stainless steel fixed-bed flow reactor with a quartz lining. About 150 mg catalyst (420-840 μm) was packed into the reactor. At first, the catalyst was reduced in pure H_2 at a flow rate of 30 ml/min at 300ºC for 1 h under atmospheric pressure. A gas mixture (24% CO_2, 72% H_2 and 4% N_2) with a flow rate of 15 ml/min was introduced into the reactor

after the temperature was decreased to 50ºC. The CO_2 hydrogenation reaction was performed at 3.0 MPa and various temperatures between 190 and 240ºC. For comparison with commercial CuZnAl catalyst, 50 mg catalyst with a particle size around 100-150 μm was diluted by 300 mg quartz sand and tested in a reaction gas flow rate of 20 ml/min. The outlet gases were passed through the cold trap and then analyzed by two online gas chromatographers (GC), one is equipped with a TCD detector (SHIMADZU GC-8A) and the other is equipped with a flame ionization detector (FID, SHIMADZU GC-14C). The CO_2 conversion and CH_3OH selectivity were obtained from the GC data.

$$X_{CO_2} = \frac{F_{CO_2,in} - F_{CO_2,out}}{F_{CO_2,in}}$$

$$S_{CH_3OH} = \frac{F_{CH_3OH,out}}{F_{CO_2,in} - F_{CO_2,out}}$$

$$S_{CO} = \frac{F_{CO,out}}{F_{CO_2,in} - F_{CO_2,out}}$$

$$\text{Methanol yield } (g_{CH_3OH} \cdot kg_{Cu}^{-1} \cdot h^{-1}) = \frac{F_{CO_2} \times X_{CO_2} \times S_{CH_3OH} \times 32 \times 60}{22.4 \times m_{cat} \times x_{Cu}}$$

X_{CO_2} is the conversion of CO_2. S_x is the selectivity of x species in products. $F_{x,in}$ and $F_{x,out}$ are the inlet and outlet flow rates of x species (ml/min), respectively. X_{CO_2} is the conversion of CO_2. S_x is the selectivity of x species in products. $F_{x,in}$ is the inlet flow rate of x species (ml/min), $F_{x,out}$ is the outlet flow rate of species x (ml/min). m_{cat} is the amount of catalyst, x_{Cu} is the Cu content in catalysts.

Catalyst characterizations

The phase composition of the catalyst was identified by X-ray powder diffraction (XRD) on a PANalytical X'Pert diffractometer with Cu-Kα (40 kV, 40 mA) radiation. The content of Cu in the as-prepared catalyst was detected by an inductively coupled plasma optical emission spectrometer (ICP-OES, 7300DV). The Cu content of commercial CuZnAl was evaluated to be 55.6 wt% by XRF (Zetium). Transmission electron microscopy (TEM) images were obtained on JEM-2100 system (JEOL) with an acceleration voltage of 200 kV. The sample was ultrasonically suspended in ethanol and placed onto a carbon film. The metallic copper surface area (S_{Cu}) was determined by using N_2O oxidant followed by TPR on BELCAT II chemisorption analyzer (MicrotracBEL, Corp.) according to the procedure described elsewhere[3]. The catalysts were firstly reduced in a 10% H_2/Ar mixture (50 ml/min) with a temperature reduction program (TPR) from room temperature to 500ºC at a ramping rate of 10ºC /min. Then the reactor was purged with Ar and cooled down to room temperature. The amount of H_2 consumption in the first TPR was denoted as X. After that, the catalyst was exposed to 5% N_2O/N_2 (50 ml/min) at 50ºC for 30 min. The reactor was purged with Ar to remove the surface oxidants. Finally, the second TPR was operated in the same procedure as the first time, and H_2 consumption in the second TPR was denoted as Y. Dispersion (D_{Cu}), Cu surface area (S_{Cu}) and average

volume-surface diameter (d_{Cu}) were calculated by D_{Cu} =2X / Y ×100%, S_{Cu} = 2Y × N_{av} / (X × M_{Cu} × 1.4 × 10^{19}) (m^2_{Cu}/g_{Cu}) and d_{Cu} =0.5 × X / Y (nm), respectively, where N_{av} is Avogadro's constant; M_{Cu} is the relative atomic mass of copper (63.46 g/mol); 1.47 × 10^{19} is the number of Cu atom of per square meter. Temperature programmed desorption of H_2 (H_2-TPD) experiment was performed on Autochem II 2920 (Micromeritics Corp.) with OmniStar mass spectrometer (MS, PFEIFFER). Before the adsorption, 30 mg of the sample was pre-treated in He stream at 300ºC for 45 min to remove the absorbance on the surface of catalysts and then reduced by H_2 at 300°C for 1 h. After cooling down to 50ºC, the sample was purged by Ar at 50ºC for 30 min. Subsequently, the H_2 desorption was carried out from 50 to 900ºC with a heating rate of 10ºC/min in the He stream (50 ml/min). The H_2 signal (m/z = 2) during the desorption process was recorded by a Pfeiffer OmniStar mass spectrometer. H_2-D_2 isotopic exchange experiments were conducted on BELCAT II (MicrotracBEL, Corp) with OmniStar MS (PFEIFFER). Catalysts were reduced at 300°C for 45 min and flushed by He for another 45 min. Then catalysts were stabilized in 5% H_2/Ar (30 ml/min) at 230°C. Finally, the gas was switched into a mixture of 2.5% H_2/2.5%D_2/Ar until the singals of HD (m/z = 3) and D_2 (m/z = 4) were stable. After each test, the gas was directly introduced into MS without going through the samples for calibration. The percentage of H/D exchange was evaluation according to the MS signals of calibrated D_2 and balanced D_2 at the stable stage.

The X-ray absorption spectroscopy (XAS) experiments were performed at the CAT-ACT beamline at the KIT Light Source[4]. The catalyst powder (sieve fraction 100-200 μm, 1:1 diluted with cellulose) was loaded in a tailor-made stainless steel high-pressure cell for XAS measurements[5]. The pressure was adjusted using electronic regulators (Schuster Creative Systems; N802 motors by GULEX, Germany) which were controlled by two process controllers (PMA KS 90-1). XAS spectra were recorded in transmission mode at Cu K-edge (8979 eV), Zn K-edge (9659 eV) and Zr K-edge (17998 eV) using a double-crystal Si(111) monochromator. Cu, Zn and Zr reference foils mounted between the second and third ionization chamber were measured simultaneously for absolute energy calibration. Operando XANES measurements during the reduction, adsorption and reaction process were carried out step by step as shown in Figure S12. For the first TPR step, the sample was heated in 75% H_2/He at a flow rate of 40 ml/min up to 300 °C with a ramping rate of 5°C/min and kept stable for 30 min. Then the sample was purged with He and cooled down to 50°C for EXAFS measurements (denoted as after reduction). The temperature and pressure were increased to 230 °C and 2.1 MPa, respectively. For the CO_2 adsorption step, the gas was changed into 50 % CO_2/He (20 ml/min) and kept stable for 30 min. In the following step, CO_2 hydrogenation reaction was conducted in 25 % CO_2/H_2 (40 ml/min) for 60 min at the same temperature and pressure. The component of outlet gas was simultaneously analyzed by an online micro gas chromatograph (μ-GC, Agilent 490; channel 1: 10 m PoraPLOT Q, 0.25 mm diameter, carrier gas He; channel 2: 10 m mole sieve column with 5Å, 0.25 mm diameter, carrier gas Ar). The

XANES spectra up to k = 8 Å^{-1} were recorded every 4 min for Cu and Zn during the whole process. EXAFS spectra up to k = 12 Å^{-1} for as-prepared, reduced and spent samples were measured at 50°C. All of the data were processed and analyzed using the IFFEFIT software package[6]. The EXAFS equation[7] used for deriving the free parameters is given by

$$\chi(k) = S_o^2 \sum_i N_i \frac{f_i(k)}{kR_i^2}\ e^{-\frac{2R_i}{\lambda(k)}}\ e^{-2k^2\sigma_i^2}\ sin(2kR_i + \delta_i(k))$$

where, S_o^2 is the amplitude reduction factor, N is the degeneracy of the scattering path, f(k) is the scattering function, k is the wavenumber, R is the distance between absorber and scatterer, λ is the mean free path of the photoelectron, σ^2 is the mean square radial displacement also known as Debye-Waller factor, δ is the phase shift of the couple absorber/scatterer and i represents a particular number of shell. R-factor represents the goodness of fit. The time-resolved XAS spectrum was analyzed by linear combination fitting (LCF). The first spectra (denoted as ZnO) and Zn foil were used as standards.

We employed dispersion-corrected density-functional theory (DFT-D3)[8] and the plane-wave method to compute the structures and energetics. The projector-augmented-wave (PAW)[9] method in conjunction with the generalized gradient-approximation (GGA) was used to determine the dispersion forces and energy. Perdew-Burke-Ernzerhof functional implemented in Vienna Ab Initio Simulation Package (VASP)[10] was adopted to compute the exchange-correlation potentials. The kinetic energy cut-off was 500 eV for plane wave basis set. DFT+U approach were used to compensate the inherent errors of on-site electron interactions in PBE functional, with Hubbard-U parameters of 4.7 eV for Zn and 4.0 eV for Zr. The DFT+U approach has been verified to represents good compromise between accuracy and computational cost[11]. D3 method developed by Grimme and coworkers[8] provided accurate description for molecular adsorption interaction on metal surfaces than ordinary density functional methods, as the C_6 parameters are improved utilizing time-dependent density functional calculations, and the parameters can be optimized according to the local chemical environment with the use of fractional coordination numbers. The climbing-image nudged elastic band (CI-NEB) technique implemented in VTST program[12] was applied to find the saddle points and construct the potential-energy profile. The copper cluster exhibits (111) surface. A quite large $\left(\frac{7\sqrt{2}}{2} \times 5\right)$R45° supercell was used to represent the non-polar ZrO_2 (100) substrate. The bottom two ZrO_2 layers were fixed to mimic their bulk properties. The top oxide layers and the copper clusters were relaxed until atomic forces smaller than 0.02 eV Å^{-1} with the conjugated-gradient method. A large vacuum layer of 17 Å was imposed between different layers in order to avoid chemical interactions between adjacent periodic images.

In situ diffuse reflectance infra-red Fourier transform spectroscopy (DRIFTS) results at atmosphere pressure were carried out on a Bruker VERTEX 70 Fourier transform IR spectrometer. The sample was

pretreated in pure H_2 flow (20 ml/min) for 30 min at 300ºC and then purged with He flow (20 ml/min) for 30 min. After that, the sample was decreased to 230°C, where the background spectrum (200 scans) with a resolution of 4 cm^{-1} was obtained. The inlet gas was firstly switched into 30% CO_2/H_2 at 20 ml/min for 30min and then changed into He (20 ml/min) for 30min. Infrared spectra were collected every 2.5 min in the Kubelka-Munk mode. The spectra were reported in Kubelka Munk units by converting with the following formula:

$$F(R_\infty) = \frac{(1 - R_\infty)^2}{2R_\infty}$$

where R_∞ stands for the reflectance of the sample (measured relative to the sample under Ar as background scan).

Operando DRIFTS experiments at high pressure were conducted on a Thermo Scientific Nicolet 6700. Reaction cell was PIKE Diffus IR_{TM} with a home-made high-pressure controlling system. The sample was pretreated in pure H_2 flow (30 ml/min) for 60 min at 300ºC, and then the atmosphere was switched to He flow (30 ml/min) for 60 min. After that, the sample was cooled to 230°C, where the background spectrum was obtained. The feed gas (30% CO_2/H_2) was switched into the reaction chamber, and the pressure was increased to 3.0 MPa. Infrared spectra were collected every 3.0 min in the Kubelka-Munk mode during the reaction for 90 min.

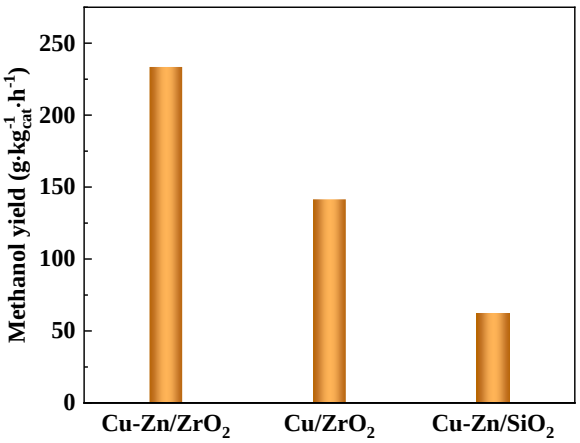

Figure S1. Methanol yield over SFSP made Cu-Zn/ZrO_2, Cu/ZrO_2 and Cu-Zn/SiO_2 for individually comparing the effects of Zn (Cu-Zn/ZrO_2 vs Cu/ZrO_2) and Zr (Cu-Zn/ZrO_2 vs Cu-Zn/SiO_2). Reaction conditions: 50 mg catalyst, 230°C, 3.0 MPa, GHSV = 24000 ml/(g_{cat}·h).

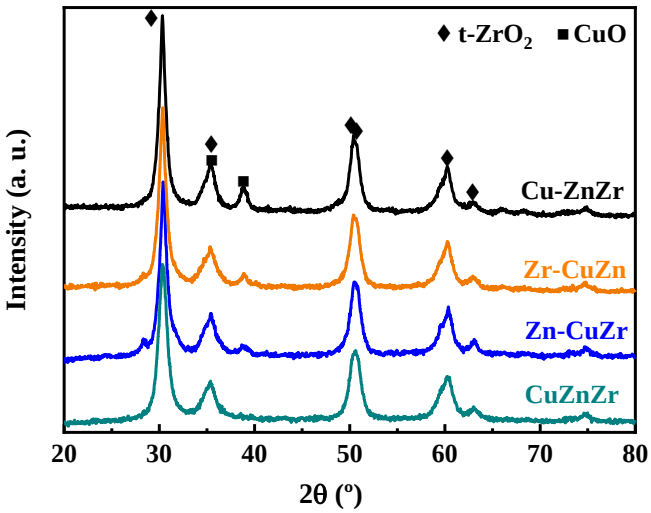

Figure S2. XRD patterns of all three as-prepared catalysts. The assigned values are taken from ICSD crystallographic data source: t-ZrO_2 (01-080-0784) and CuO (00-045-0937). The crystal structure of ZrO_2 support is tetragonal for all samples. Large Cu particles exist in Cu-ZnZr from the typical peak of CuO, because CuO particles were produced in the isolated flame without any supports. They are barely observed in the CuZnZr sample made by the single flame FSP.

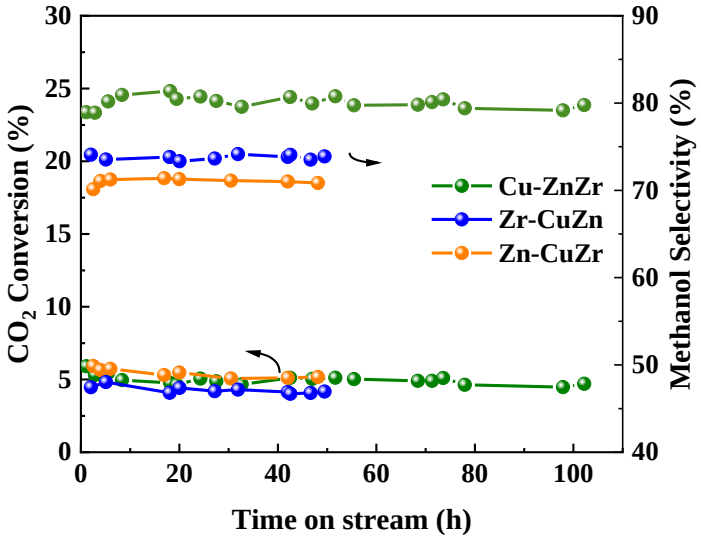

Figure S3. Stability tests over Cu-ZnZr, Zr-CuZn and Zn-CuZr catalysts for CO_2 hydrogenation to methanol. CO is the only side product over all samples during CO_2 hydrogenation. Reaction conditions: 150 mg catalyst, 220°C, 3.0 MPa, GHSV = 6000 ml /(g_{cat}·h), TOS = 50-100 h.

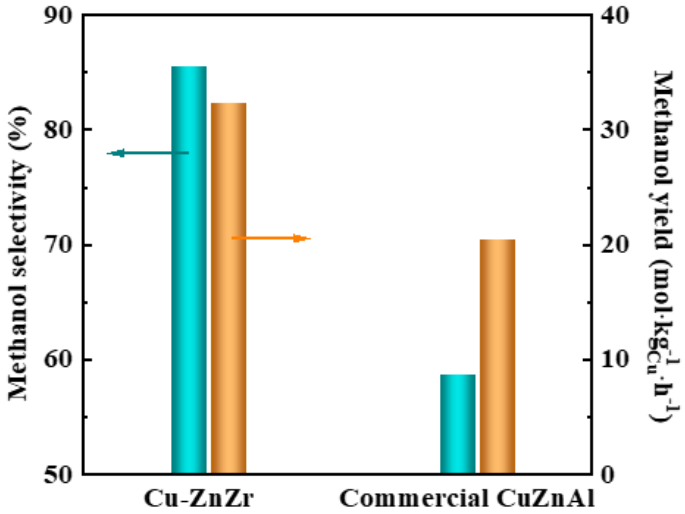

Figure S4. Methanol yield and selectivity of Cu-ZnZr sample and commercial Cu/ZnO/Al_2O_3 (CuZnAl) catalyst. Reaction conditions: 50 mg catalyst, 230°C, 3.0 MPa, GHSV = 24000 ml/(g_{cat}·h).

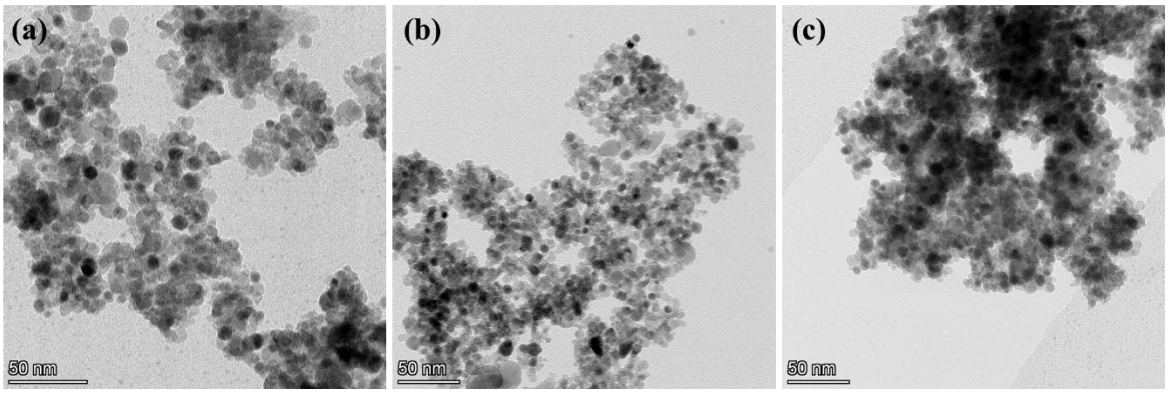

Figure S5. TEM images of as-prepared (a) Cu-ZnZr, (b) Zr-CuZn and (c) Zn-CuZr catalysts.

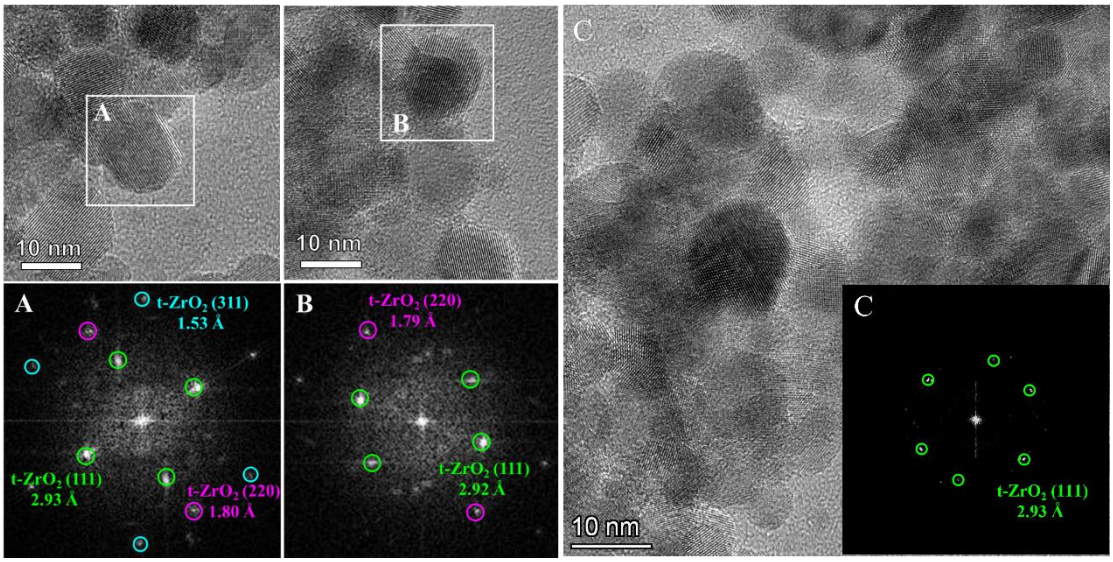

Figure S6. TEM images of reacted Cu-ZnZr catalyst and Fast Fourier Transform (FFT) analysis of the selected area.

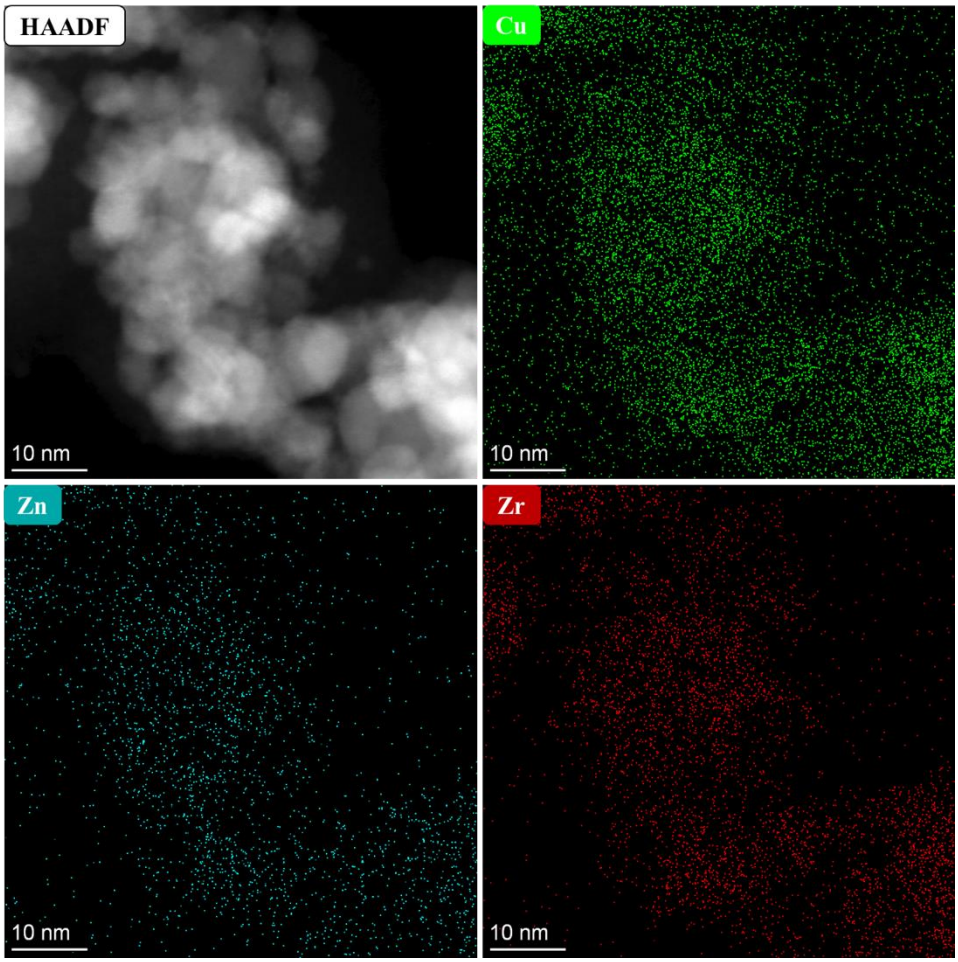

Figure S7. High-angle annular dark-field (HAADF) image and EDX mapping of Cu, Zn and Zr elements of reacted Cu-ZnZr catalyst.

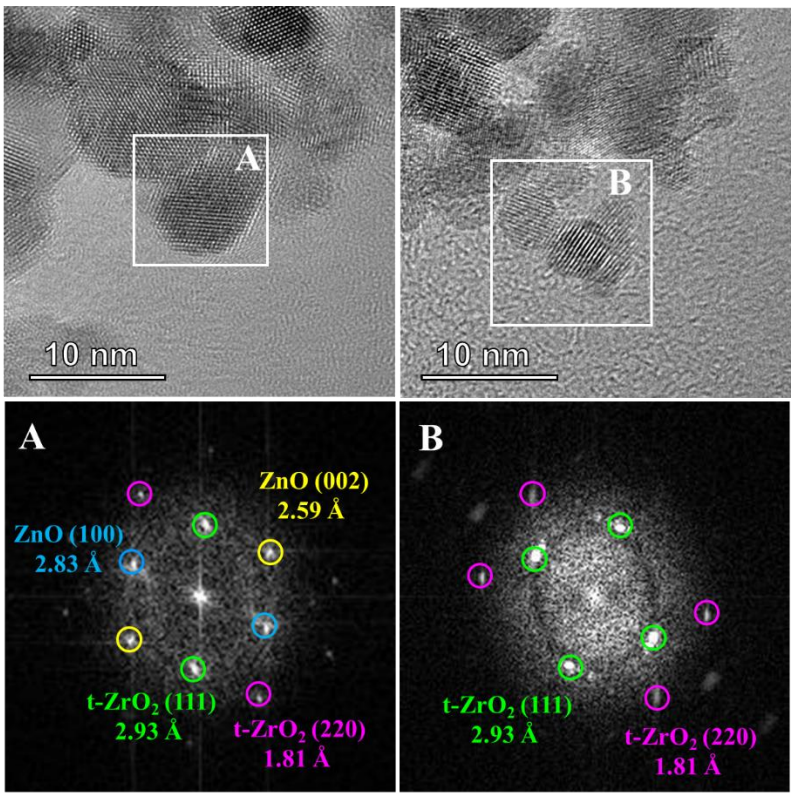

Figure S8. TEM images of reacted Zr-CuZn catalyst and FFT analysis of the selected area.

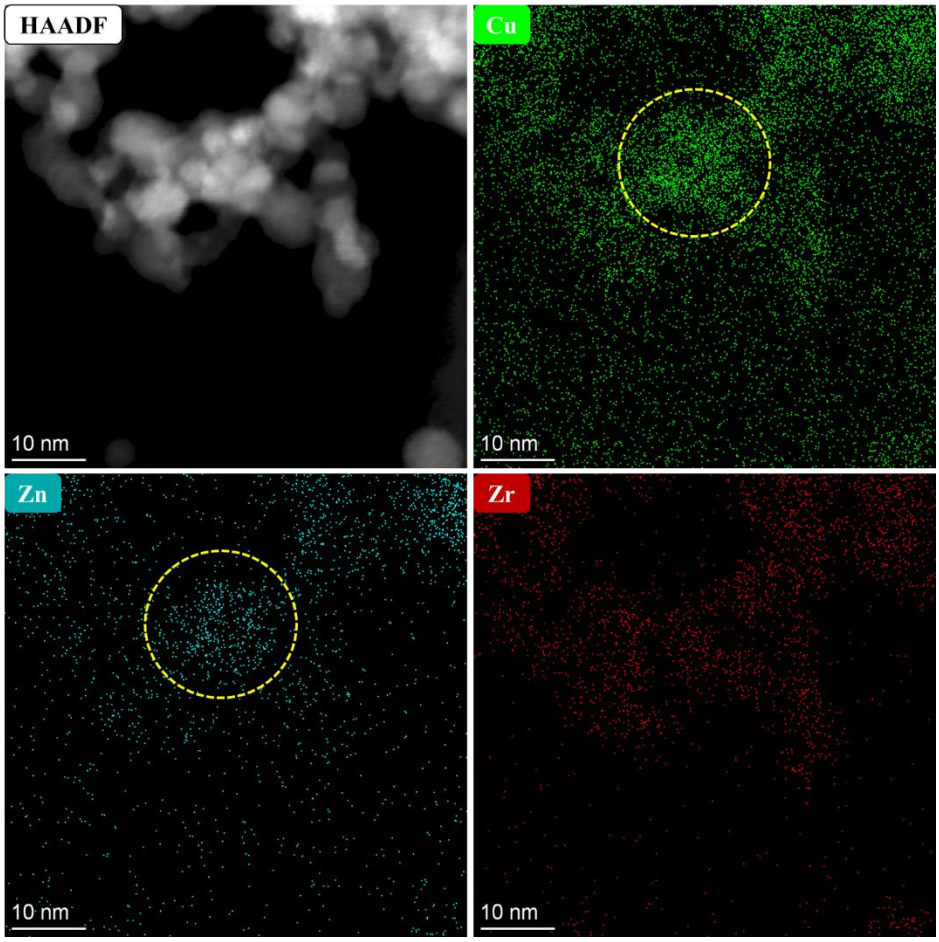

Figure S9. High-angle annular dark-field (HAADF) image and EDX mapping of Cu, Zn and Zr elements of reacted Zr-CuZn catalyst. The dotted circle represents intimate contact between Cu and ZnO.

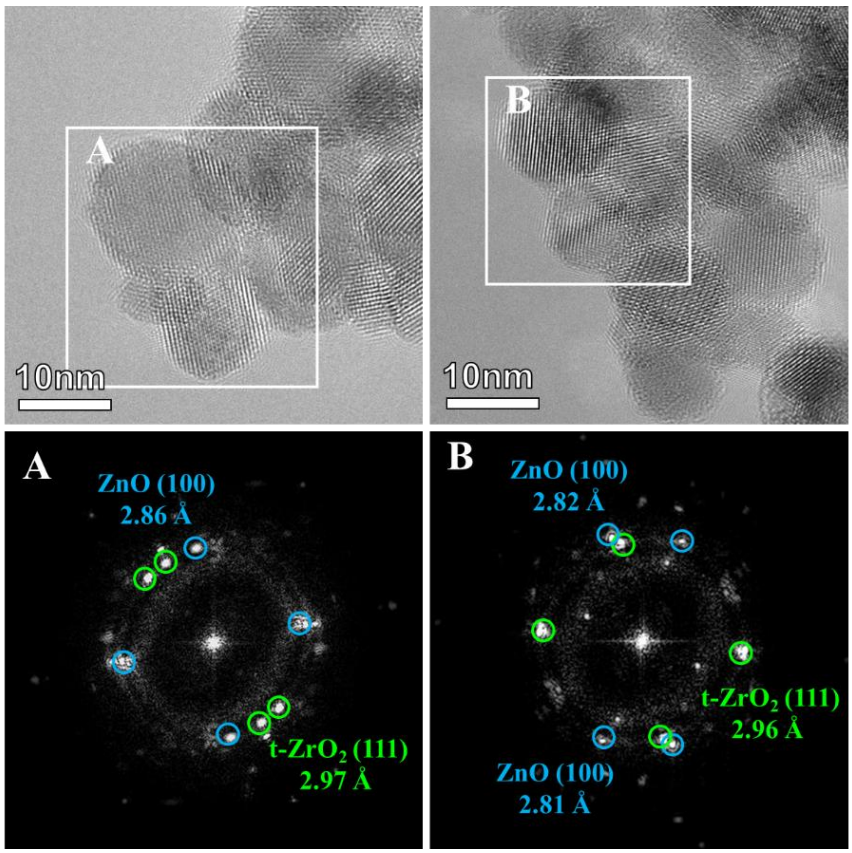

Figure S10. TEM images of reacted Zn-CuZr catalyst and corresponding FFT analysis of the selected area.

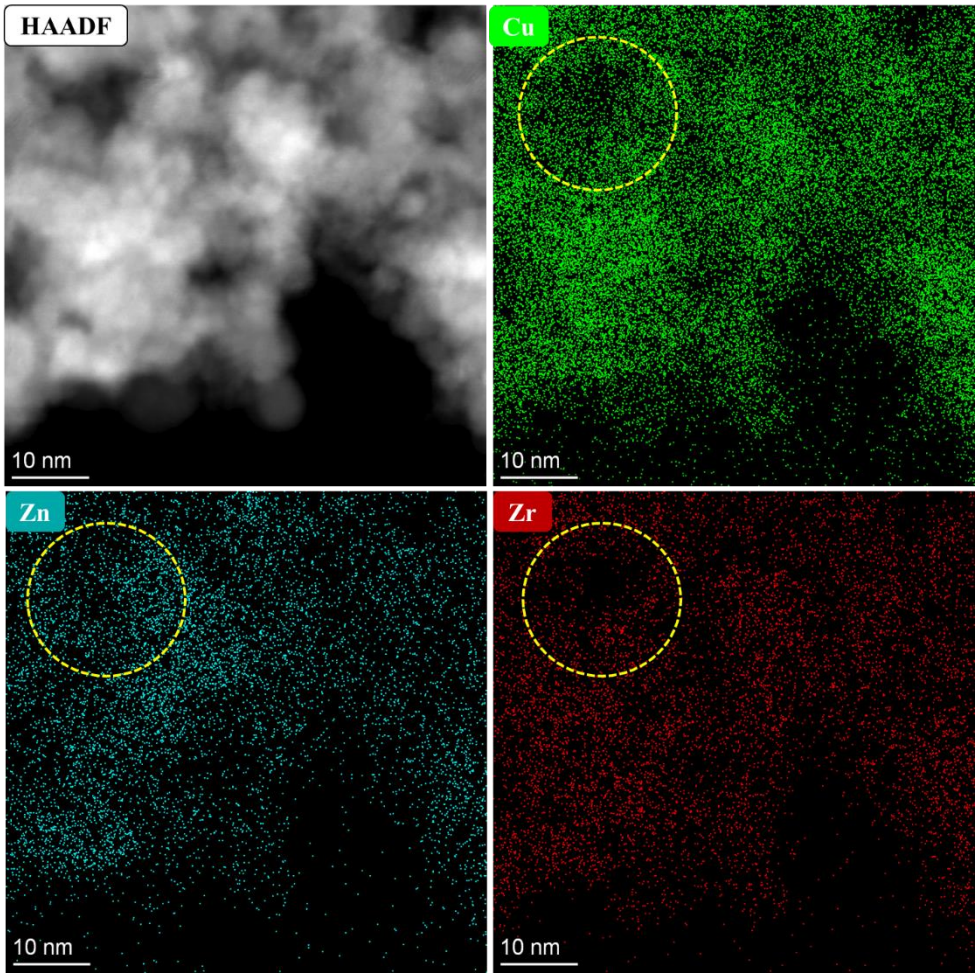

Figure S11. High-angle annular dark-field (HAADF) image and EDX mapping of Cu, Zn and Zr elements of reacted Zn-CuZr catalyst, where isolated ZnO nanoparticles without interaction with Cu and Zr were observed and marked by yellow circles in the figure.

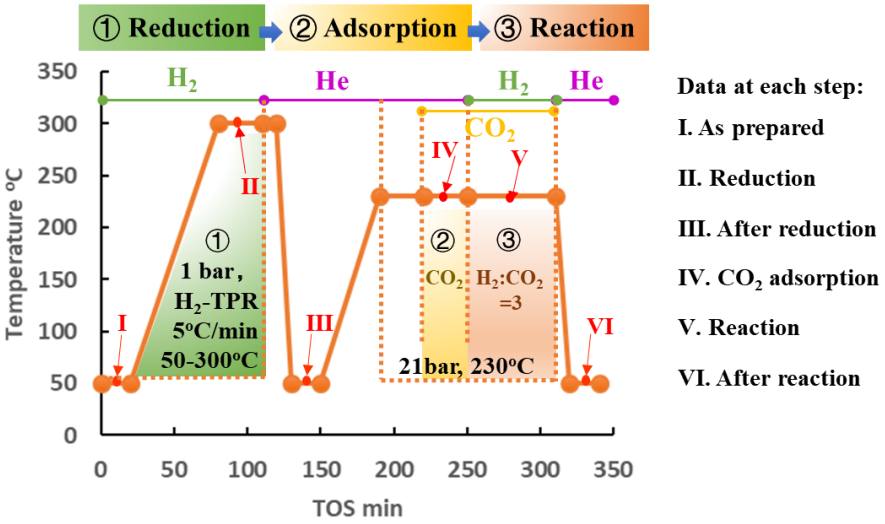

Figure S12. Process of in situ/operando conditions. EXAFS spectra of the initial state were firstly recorded at 50°C (I). H_2-TPR was conducted with a ramping rate of 5°C/min from 50 to 300°C (II). After holding 30 min, the atmosphere was changed from H_2 to He, following the cooling process to 50 °C (III). Then, the samples were heated to 230°C at 2.1 MPa and 25 vol% CO_2/He was introduced for 30 min (IV). In the next step, the reaction was conducted with an H_2/CO_2 ratio of 3:1 at the same condition for 60 min (V). Finally, the temperature was cooled down to 50°C with a He sweep (VI). During the reaction process, outlet gas was analyzed by an online GC to evaluate the relationship between Zn species and the catalytic performance under real reaction conditions.

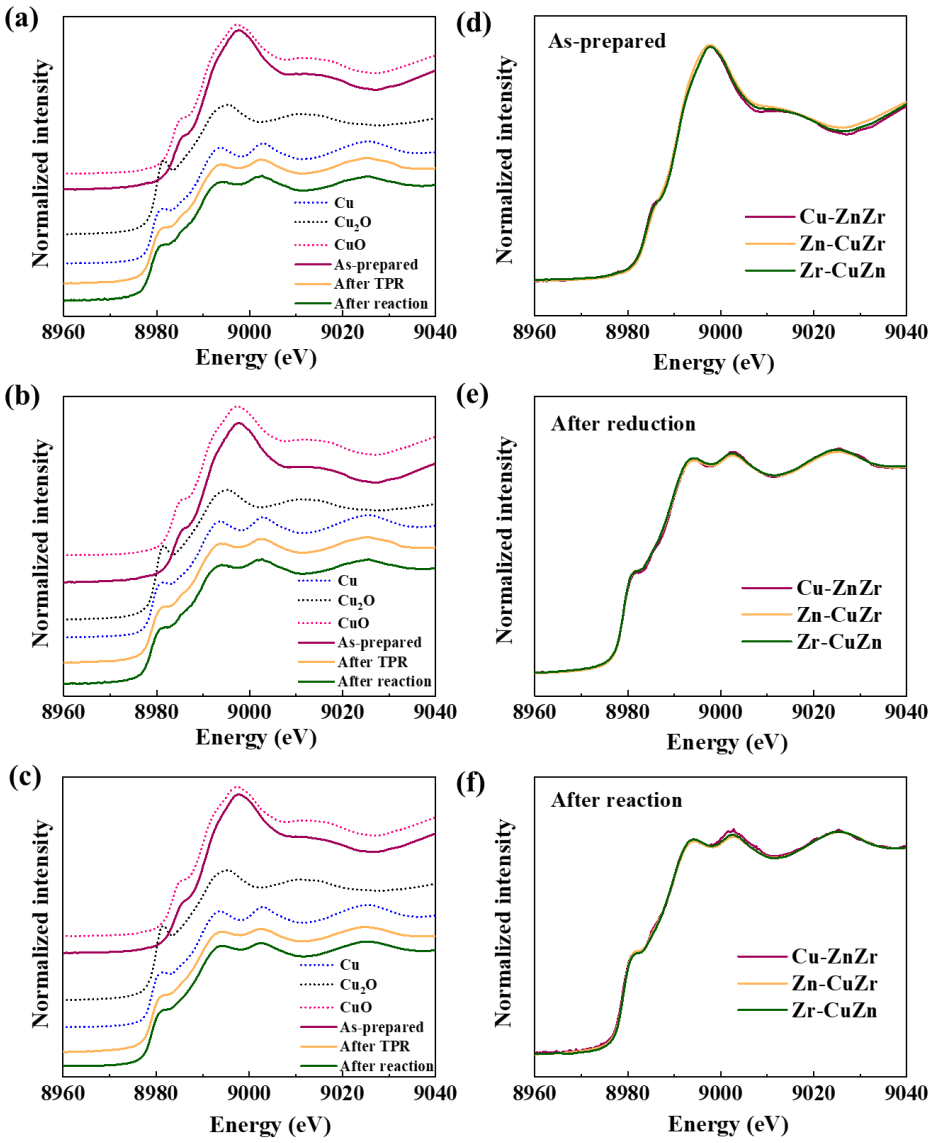

Figure S13. XANES spectra at Cu K-edge for (a) Cu-ZnZr, (b) Zr-CuZn and (c) Zn-CuZr samples before treatment (as-prepared), after TPR and after reaction, as well as standard spectra of Cu, Cu_2O and Cu. Comparison of XANES spectra at Cu K-edge for the samples at different stages: (d) as-prepared, (e) after TPR and (f) after the reaction.

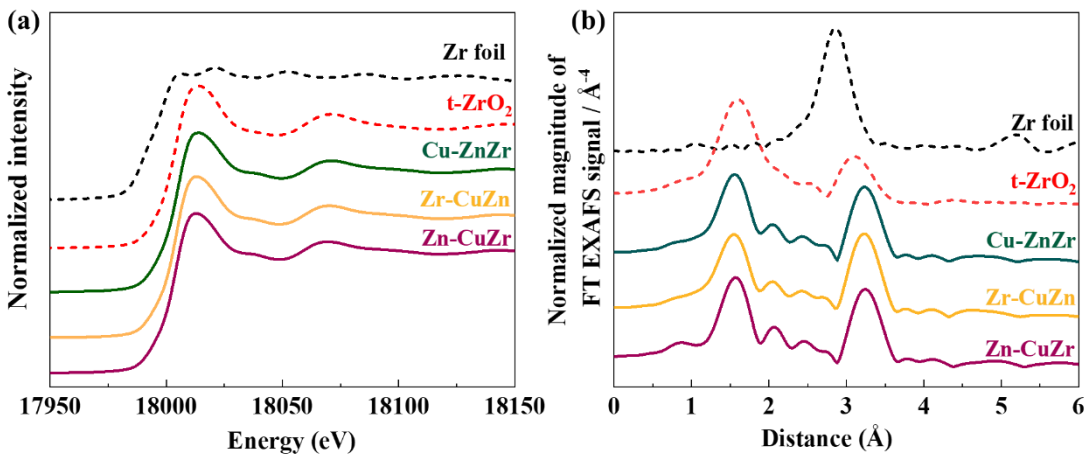

Figure S14. XAS spectra of the as-prepared samples, as well as the standard spectra of Zr foil and ZrO_2 reference: (a) XANES spectra at the Zr K-edge and (b) FT magnitude of the k^3-weighted Zr K-edge EXAFS spectra.

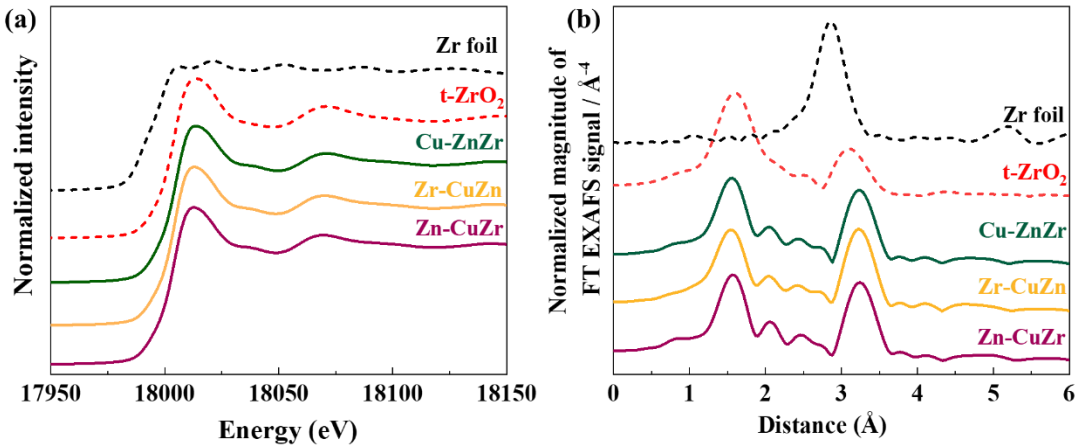

Figure S15. XAS spectra of the reacted catalysts, as well as the standard spectra of Zr foil and ZrO_2 reference: (a) XANES spectra at the Zr K-edge and (b) FT magnitude of the k^3-weighted Zr K EXAFS spectra.

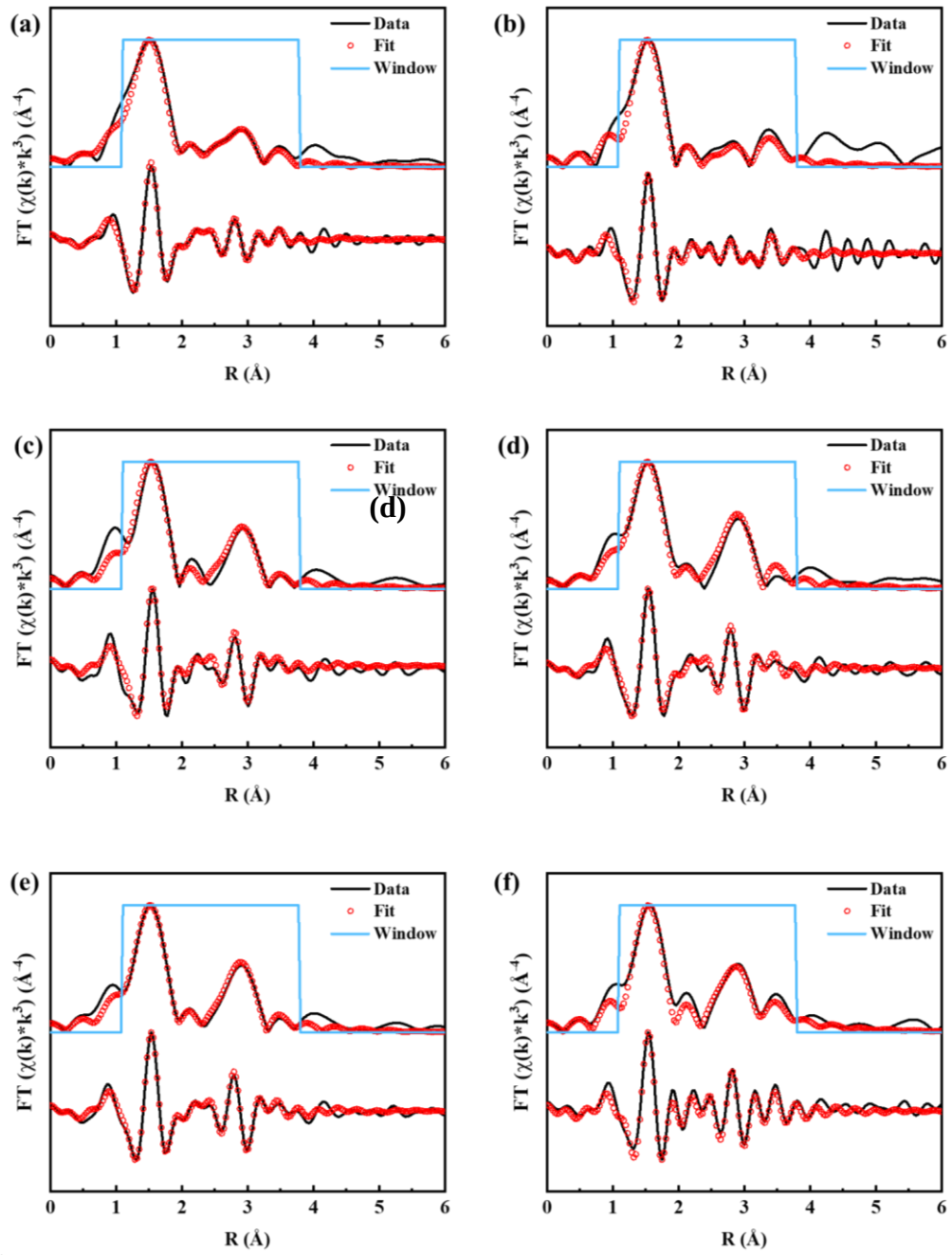

Figure S16. k^3-weighted Fourier transformed EXAFS (black) and the fitted spectrum (red) at the Zn K-edge of (a, c, e) as-prepared and (b, d, f) reacted (a, b) Cu-ZnZr, (c, d) Zr-CuZn and (e, f) Zn-CuZr catalysts.

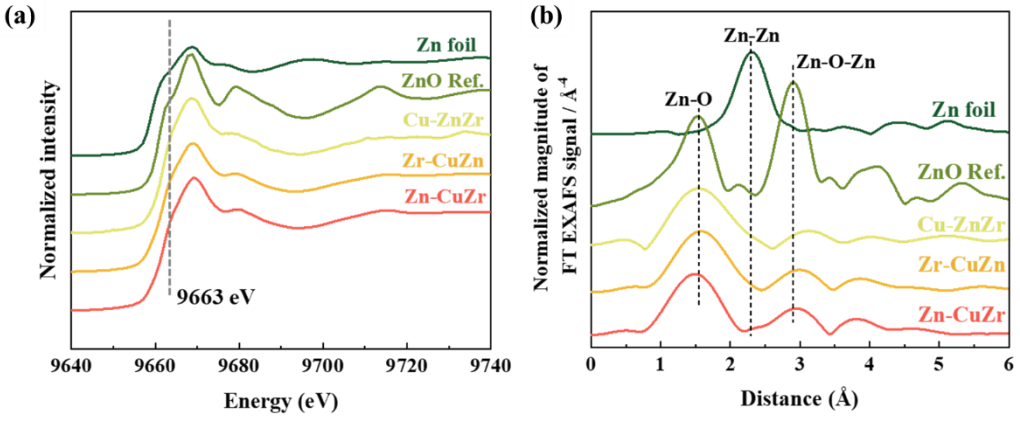

Figure S17. Normalized XANES spectra at Zn K-edge of all the reduced (a and b) samples, compared with standard spectra of Zn foil and ZnO reference.

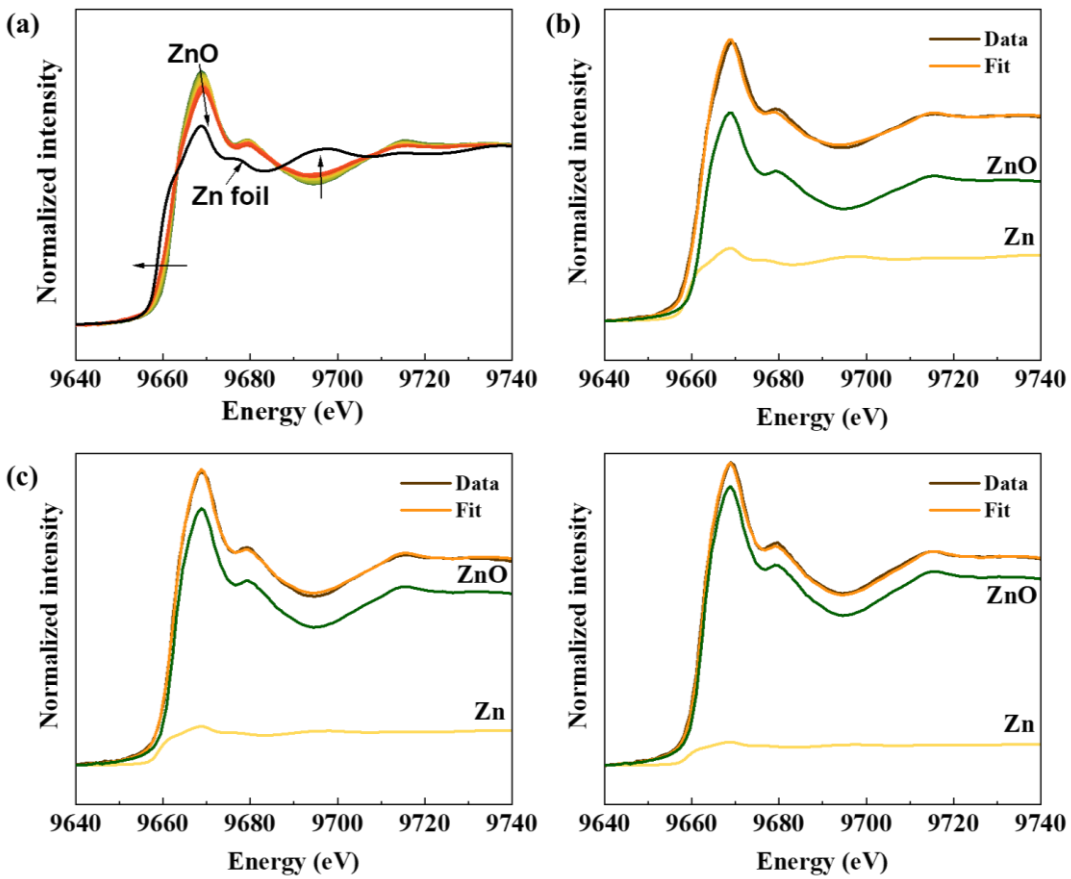

Figure S18. (a) Variations of Zn K-edge XANES spectra during reduction process; Results of linear combination fitting (LCF) of XAS spectra of Zn-CuZr catalyst (b) after the TPR process (R factor=0.002), (c) after the CO_2 adsorption (R factor=0.001) and (d) after the CO_2+H_2 reaction (R factor=0.001).

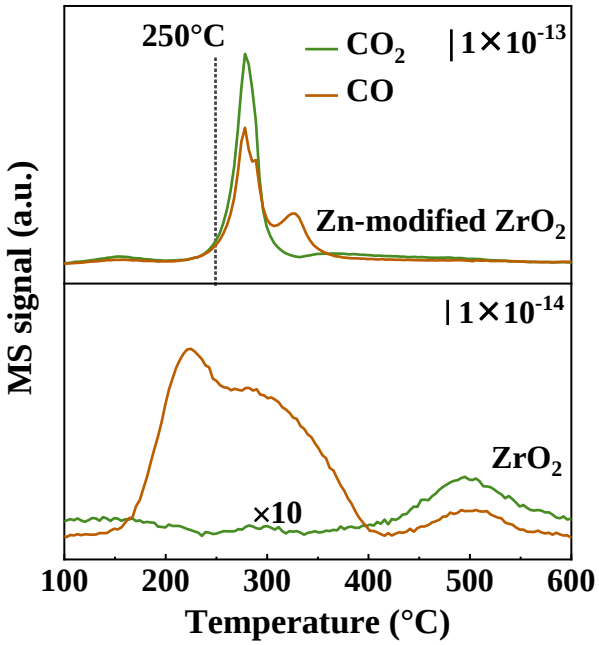

Figure S19. HCOOH-TPD of FSP-made Zn modified ZrO_2 support and ZrO_2 support.

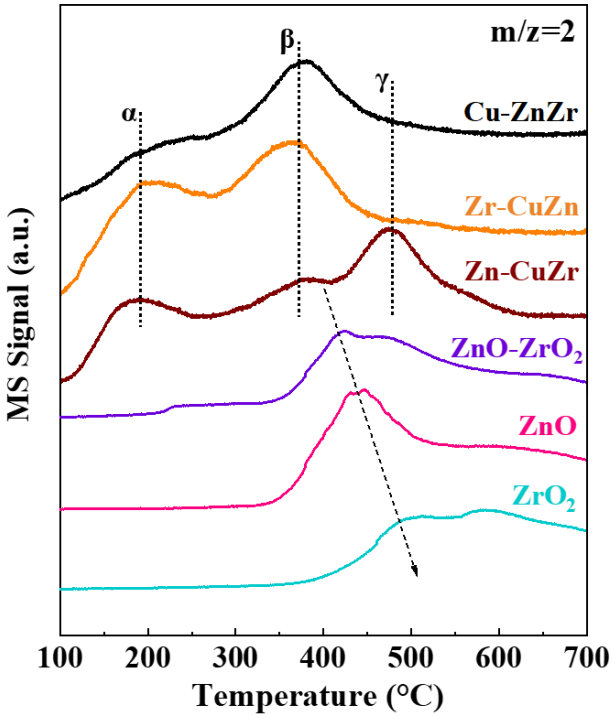

Figure S20. H_2-TPD of three DFSP-made Cu-Zn-Zr ternary catalysts and SFSP-made ZnO-ZrO_2, ZrO_2 and ZnO as references.

Note: Compared to the oxides samples, peak α below 200°C belongs to the active H species created by Cu, but they are too active and unstable to contribute to reaction[13]. The active β hydrogen for the hydrogenation from formate to methoxy[14] is created on the Cu-Zn interface, which is hard to be obtained in the Zn-CuZr catalyst due to the separation of Cu and Zn. Most of the hydrogen is desorbed at high temperatures as peak γ in Zn-CuZr, which has limited contributions to the reaction. Thus the formate hydrogenation to methanol is hard to proceed on the Zn-CuZr catalyst because of the lack of active hydrogen, which is consistent with the lowest methanol selectivity and the DRIFTS results.

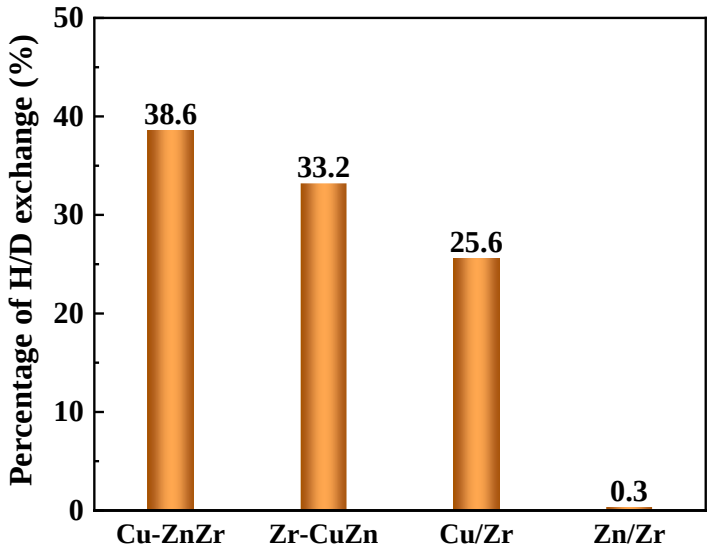

Figure S21. Results of H_2-D_2 isotopic exchange experiments over DFSP made Cu-ZnZr and Zr-CuZn samples, as well as Cu/ZrO_2 (Cu/Zr) and ZnO-ZrO_2 (Zn/Zr) made by SFSP method for comparison.

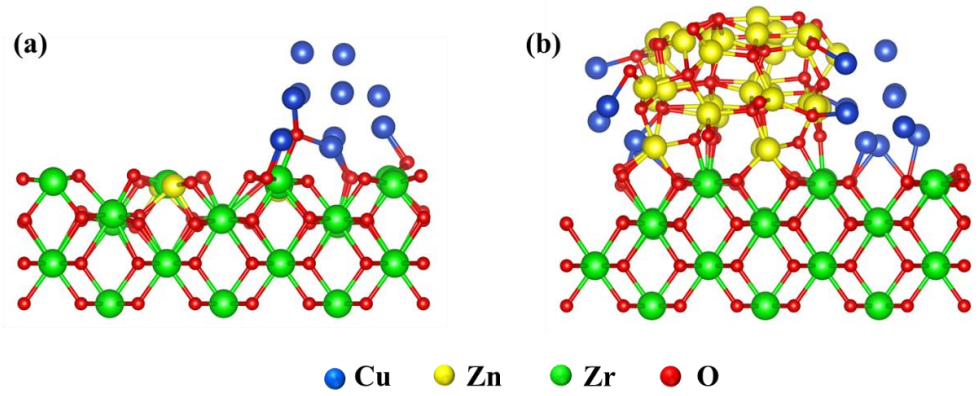

Figure S22. Fabrication of Model 1 (a) and Model 2 (b) for DFT calculation based on Cu-ZnZr and Zr-CuZn catalysts, respectively.

Note: In Model 1, part of Zr atoms is replaced by Zn atoms to construct atomically dispersed Zn sites on ZrO_2 support, and Cu nanoparticles are located on the surface of the preformed Zn-Zr species. In Model 2, the ZnO clusters surrounded with Cu nanoparticles are fabricated in consideration of a strong Cu-Zn interface, then the Cu-ZnO particles are overall interacted with ZrO_2 support. Cu nanoparticles consisting of 16-18 Cu atoms in above models are used according to the Cu particle diameters (2-6 nm) from experimental analysis in Table S1.

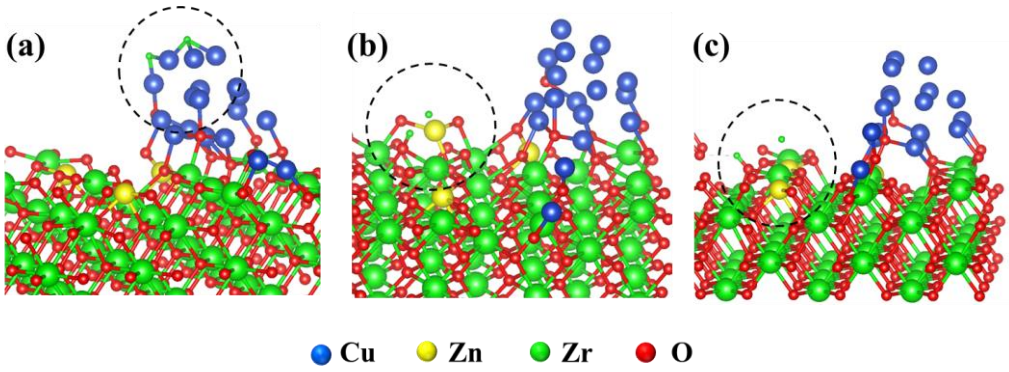

Figure S23. H_2 dissociation states on surface of metallic Cu sites (a), atomically dispersed Zn sites (b) and Zr sites on the surface of ZrO_2 support (c) in Model 1 for DFT calculation based on Cu-ZnZr sample.

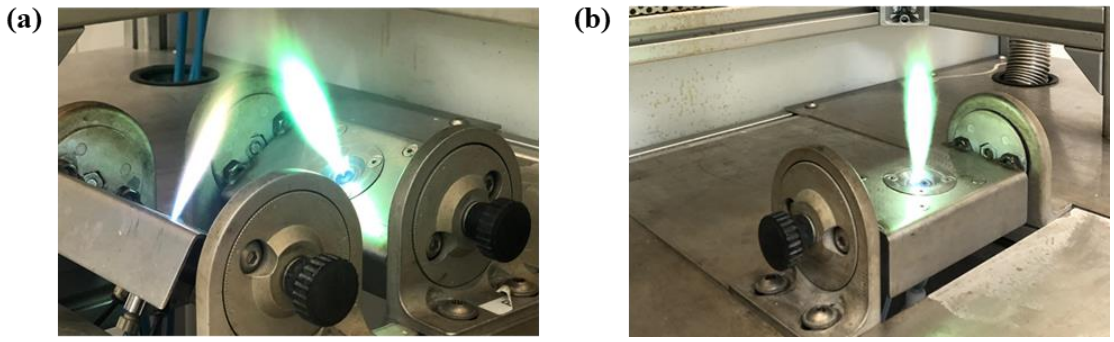

Figure S24. Photos of (a) DFSP and (b) SFSP preparation setups.

Table S1. Textural and structural properties of all catalysts

Catalysts	CuO (wt.%)[a]	ZnO (wt.%)[a]	ZrO_2 (wt.%)[a]	S_{Cu} (m^2/g_{Cu})[b]	D_{Cu} (%)[c]	Particle size (nm)[d]
Cu-ZnZr	21.0	8.0	71.0	105.6	15.6	6.4
Zr-CuZn	21.5	7.5	71.0	199.2	29.5	3.4
Zn-CuZr	19.5	7.6	72.9	238.2	35.2	2.8
CuZnZr	19.6	7.2	73.2	270.0	39.9	2.5

[a]Contents in fresh catalysts was determined by ICP-OES.

[b]Cu surface area was determined by N_2O oxidation followed by TPR method[3].

[c]Cu dispersion was calculated according to Cu surface area.

[d]Cu particle size was calculated according to Cu dispersion.

Table S2. Comparison of the catalytic performance of Cu-ZnZr with some typical $Cu/ZnO/Al_2O_3$ (CZA) catalysts in literatures

[a]CZA (CuZnAl) in this work is purchased from AILLY corp, where CuO, ZnO and Al_2O_3 are 69.0, 19.3 and 10.9 wt%, respectively.

Catalysts	Cu content (wt.%)	P (MPa)	T (°C)	Methanol Sel. (%)	CO_2 Conv. (%)	GSHV ($mL/g_{cat}\cdot h^{-1}$)	Methanol STY ($g\cdot kg_{cat}^{-1}\cdot h^{-1}$)	Methanol ($g\cdot g_{Cu}^{-1}$
Cu-ZnZr	15.6	3.0	230	86.0	2.5	24000	177.0	1.1
CZA[a]	55.2	3.0	230	58.7	7.8	24000	377.6	0.7
CZA[a]	55.2	4.5	225	70.2	8.5	42000	850.7	1.6
e-made CZA[15]	31.9	3.0	230	43.0	18.7	2400	68.8	0.2
ZA-Sanju[16]	\	2.0	320	33.0	20.5	6000	*ca.* 105.6	\
-KATALCO[17]	50.0	2.0	270	*ca.* 44	*ca.* 2.2	67500	186.6	0.4
A-Alfa Aesar[18]	46.5	4.5	220	77.0	8.1	37600	827.0	1.7

Table S3. Infrared band assignments of the surface species for the CO_2 + H_2 reaction.

Surface species	Wavenumber (cm^{-1})
Formate (HCOO*)[19]	2982-2978, 2878-2874, 2732-2726, 1620-1616, 1385, 1358
Methoxy (CH_3O*)[20]	2936-2931, 2830-2827
Carbonates or bicarbonate species[21]	1525, 1507, 1490, 1330

Table S4. Comparison of reaction path and energy difference for hydrogen dissociation over different sites and models. The energy difference of the second reaction path is defined as activation energy of H_2 activation.

Order	Reaction paths	Energy difference (ΔE / eV)			
		Sites in Model 1			Sites in Model 2
		Cu	Zn	Zr	Zn
1	$* + H_2 \rightarrow *H_2$	-0.4	-0.097	0.013	-0.442
2	$*H_2 \rightarrow$ TS	0.542	0.148	0.439	0.477
3	TS* → H-H	-1.39	-0.476	-0.346	-1.042

References:

[1] a) A. M. Gänzler, M. Casapu, F. Maurer, H. Störmer, D. Gerthsen, G. Ferré, P. Vernoux, B. Bornmann, R. Frahm, V. Murzin, M. Nachtegaal, M. Votsmeier, J.-D. Grunwaldt, *ACS Catal.* **2018**, *8*, 4800-4811; b) M. Tepluchin, D. K. Pham, M. Casapu, L. Mädler, S. Kureti, J.-D. Grunwaldt, *Catal. Sci. Technol.* **2015**, *5*, 455-464.

[2] a) R. Ahmad, M. Hellinger, M. Buchholz, H. Sezen, L. Gharnati, C. Wöll, J. Sauer, M. Döring, J.-D. Grunwaldt, U. Arnold, *Catal. Commun.* **2014**, *43*, 52-56; b) K. Schuh, W. Kleist, M. Høj, V. Trouillet, A. D. Jensen, J. D. Grunwaldt, *Chem. Commun.* **2014**, *50*, 15404-15406.

[3] C. J. G. V. D. GRIFT, A. F. H. WIELERS, B. P. J. JOGHI, J. V. BEIJNUM, M. D. BOER, M. VERSLUIJS-HELDER, J. W. GEUS, *JOURNAL OF CATALYSIS* **1991**, *131*, 178-189.

[4] a) A. Zimina, K. Dardenne, M. A. Denecke, J. D. Grunwaldt, E. Huttel, H. Lichtenberg, S. Mangold, T. Pruessmann, J. Rothe, R. Steininger, T. Vitova, *Journal of Physics: Conference Series* **2016**, *712*, 012019; b) A. Zimina, K. Dardenne, M. A. Denecke, D. E. Doronkin, E. Huttel, H. Lichtenberg, S. Mangold, T. Pruessmann, J. Rothe, T. Spangenberg, R. Steininger, T. Vitova, H. Geckeis, J.-D. Grunwaldt, *Rev. Sci. Instrum.* **2017**, *88*, 113113.

[5] a) M. Loewert, M. A. Serrer, T. Carambia, M. Stehle, A. Zimina, K. F. Kalz, H. Lichtenberg, E. Saraçi, P. Pfeifer, J. D. Grunwaldt, *Reaction Chemistry & Engineering* **2020**, *5*, 1071-1082; b) L. Pandit, A. Boubnov, G. Behrendt, B. Mockenhaupt, C. Chowdhury, J. Jelic, A.-L. Hansen, E. Saraçi, E.-J. Ras, M. Behrens, F. Studt, J.-D. Grunwaldt, *ChemCatChem* **2021**, *13*, 4120-4132.

[6] B. Ravel, M. Newville, *J. Synchrotron Radiat.* **2005**, *12*, 537-541.

[7] S. Calvin, *CRC Press Taylor & Francis Group* **2013**.

[8] a) S. Grimme, J. Antony, S. Ehrlich, H. Krieg, *The Journal of Chemical Physics* **2010**, *132*, 154104; b) S. Grimme, S. Ehrlich, L. Goerigk, *Journal of Computational Chemistry* **2011**, *32*, 1456-1465.

[9] a) P. E. Blöchl, *Physical Review B* **1994**, *50*, 17953-17979; b) G. Kresse, D. Joubert, *Physical Review B* **1999**, *59*, 1758-1775.

[10] a) G. Kresse, J. Furthmüller, *Physical Review B* **1996**, *54*, 11169-11186; b) G. Kresse, J. Hafner, *Physical Review B* **1994**, *49*, 14251-14269; c) G. Kresse, J. Furthmüller, *Computational Materials Science* **1996**, *6*, 15-50; d) G. Kresse, J. Hafner, *Physical Review B* **1993**, *47*, 558-561.

[11] H. V. Thang, G. Pacchioni, *ChemNanoMat* **2019**, *5*, 932-939.

[12] a) D. Sheppard, R. Terrell, G. Henkelman, *The Journal of Chemical Physics* **2008**, *128*, 134106; b) D. Sheppard, G. Henkelman, *Journal of Computational Chemistry* **2011**, *32*, 1769-1771; c) G. Henkelman, B. P. Uberuaga, H. Jónsson, *The Journal of Chemical Physics* **2000**, *113*, 9901-9904.

[13] B. An, J. Zhang, K. Cheng, P. Ji, C. Wang, W. Lin, *J. Am. Chem. Soc.* **2017**, *139*, 3834-3840.

[14] D. Bianchi, J.-L. Gass, M. Khalfallah, S. J. Teichner, *Appl. Catal., A* **1993**, *101*, 297-315.

[15] C. Li, X. Yuan, K. Fujimoto, *Appl. Catal., A: Gen.* **2014**, *469*, 306-311.

[16] L. Wang, E. Guan, Y. Wang, L. Wang, Z. Gong, Y. Cui, X. Meng, B. C. Gates, F. S. Xiao, *Nat. Commun.* **2020**, *11*, 1033.

[17] S. Tada, K. Larmier, R. Büchel, C. Copéret, *Catal. Sci. Technol.* **2018**, *8*, 2056-2060.

[18] X. Liu, J. Luo, H. Wang, L. Huang, S. Wang, S. Li, Z. Sun, F. Sun, Z. Jiang, S. Wei, W. X. Li, J. Lu, *Angew. Chem., Int. Ed.* **2022**, *61*, e202202330.

[19] S. Kattel, B. Yan, Y. Yang, J. G. Chen, P. Liu, *J. Am. Chem. Soc.* **2016**, *138*, 12440-12450.

[20] P. G. GOPAL, R. L. SCHNEIDER, K. L. WATTERS, *J. Catal.* **1987**, *105*, 366-372.

[21] a) E. Guglielminotti, *Langmuir* **1990**, *6*, 1455-1460; b) D. Bianchi, T. Chafik, M. Khalfallah, S. J. Teichner, *Appl. Catal. A: Gen.* **1994**, *112*, 219-235.